J. Fluid Mech. (2025), *vol.* 1018, A23, doi:10.1017/jfm.2025.10509

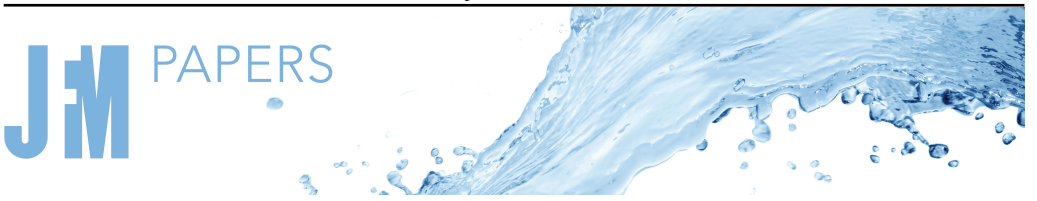

The role of motion-excited coherent structures in improved wake recovery of a floating wind turbine

Thomas Messmer[1,2], **Joachim Peinke**[1,2], **Alessandro Croce**[3] and **Michael Hölling**[1,2]

[1]Carl von Ossietzky Universität Oldenburg, School of Mathematics and Science, Institute of Physics, Oldenburg, Germany

[2]ForWind - Center for Wind Energy Research, Küpkersweg 70, Oldenburg 26129, Germany

[3]Department of Aerospace Science and Technology, Politecnico di Milano, Milan, Italy

Corresponding author: Thomas Messmer, thomas.messmer@uni-oldenburg.de

(Received 1 February 2025; revised 15 May 2025; accepted 5 July 2025)

This study experimentally investigates wake recovery mechanisms behind a floating wind turbine subjected to imposed fore-aft (surge) and side-to-side (sway) motions. Wind tunnel experiments with varying free-stream turbulence intensities ($TI_\infty \in [1.1, 5.8]$ %) are presented. Rotor motion induces large-scale coherent structures – pulsating for surge and meandering for sway – whose development critically depends on the energy ratio between the incoming turbulence and the platform motion. The results provide direct evidence supporting the role of these structures in enhancing wake recovery, as previously speculated by Messmer, Peinke & Hölling (*J. Fluid Mech.,* vol. 984, 2024, A66). These periodic structures significantly increase Reynolds shear stress gradients, particularly in the streamwise–lateral direction, which are key drivers of wake recovery. However, their influence diminishes with increasing TI_∞: higher background turbulence weakens the coherent flow patterns, reducing their contribution to recovery. Beyond a threshold turbulence level – determined by the energy, frequency and direction of motion – rotor-induced structures no longer contribute meaningfully to recovery, which becomes primarily driven by the free-stream turbulence. Finally, we show that the meandering structures generated by sway motion are more resilient in turbulent backgrounds than the pulsating modes from surge, making sway more effective for promoting enhanced wake recovery.

Key words: wakes, mixing enhancement, shear layers

1. Introduction

Early work on idealised free shear flows (jet, mixing layer, wake) showed the existence of 'large-scale orderly patterns' forming due to the amplification of small excitation (Crow & Champagne 1971; Oster & Wygnanski 1982; Cantwell & Coles 1983; Ho & Huerre 1984). These structures play a central role in the development of the flow. In the context of floating offshore wind turbines (FOWT), Li, Dong & Yang (2022), Messmer, Peinke & Hölling (2024*a*), Li, Yu & Sarlak (2024), Li & Yang (2024), Hubert, Conan & Aubrun (2025) found organised flow structures in the wake of the turbine that arise from the harmonic motion of the rotor. Numerical studies by Kleine *et al.* (2022) and Ramos-García *et al.* (2022) examined the influence of platform motion on wake dynamics under laminar wind and found that rotor oscillations lead to near-wake instabilities (Kleine *et al.* 2022), while also enhancing turbulence, mixing and energy distribution within the wake (Ramos-García *et al.* 2022). Experimental works by Rockel *et al.* (2017), Fu *et al.* (2019) and Fontanella *et al.* (2022, 2025) further support these findings. Under more realistic conditions, the intricate interactions between platform motion, inflow conditions and rotor aerodynamics result in complex wake dynamics, as explored and discussed in recent research by Bossuyt *et al.* (2023), Schliffke, Conan & Aubrun (2024), Pagamonci *et al.* (2025).

Wake recovery is a key aspect in wind energy, as it determines how the flow behind a turbine can regain lost energy through interaction with its surroundings. Li *et al.* (2022), Messmer *et al.* (2024*a*) showed in idealised conditions that rotor motion can enhance wake recovery by up to 25 % more than that of a fixed turbine. Especially for motion frequencies characterised by a platform Strouhal number $St = f_p D/U_\infty \in [0.2, 0.6]$, with f_p the platform's motion frequency, D the rotor diameter and U_∞ the incoming wind speed. They observed the formation of amplified meandering-like coherent structures from sideways rotor motion and pulsating structures from fore-aft motion, synchronised with the movements of the rotor. It remains to be seen what role these large-scale coherent structures play in the enhanced wake recovery.

Interestingly, similar wake dynamics of synchronisation and enhanced recovery are found for quite different types of harmonic excitation (actuation) on a fixed wind turbine with helix blade pitching control strategy (Frederik *et al.* 2020; Korb, Asmuth & Ivanell 2023; Van der Hoek *et al.* 2024), periodic variation of inflow structures (Mao & Sørensen 2018; Hodgson, Madsen & Andersen 2023; Wei *et al.* 2024), harmonic yaw motion (Mühle *et al.* 2024) or with dynamic variation of a turbine's thrust (Munters & Meyers 2018; Yılmaz & Meyers 2018; Croce *et al.* 2023). Combined floating platform motion and rotor excitation strategies were simulated by van den Berg *et al.* (2023), showing promising results for the coupling of wake flow mixing strategies. Several studies suggest that an optimal actuation frequency, f_a, corresponding to $St_a = (f_a D/U_\infty) \approx 0.3$, leads to the most enhanced wake recovery and the emergence of large coherent structures (Cheung *et al.* 2024). This aligns with the findings of Crow & Champagne (1971), who reported that $St_a \approx 0.3$ induces the strongest instabilities in jets. The similarity suggests that common dynamics may govern both jet flows and wind turbine wakes, as both are characterised by strong shear layers.

The papers mentioned primarily investigated harmonic excitations with idealised flow conditions (i.e. laminar). Previous studies on the wake of a fixed cylinder (Kankanwadi & Buxton 2020) and fixed wind turbine (Neunaber *et al.* 2020; Gambuzza & Ganapathisubramani 2023) analysed the impact of free-stream turbulence, characterised by the turbulence intensity ($TI_\infty = \sigma/U_\infty$) and integral length scale ($\mathcal{L}_0$) on wake mixing and development. These studies show that with increasing TI_∞, wake recovery is enhanced, due to improved mixing. The interaction between inflow turbulence and turbine harmonic excitation on wake dynamics has been studied numerically by

Yılmaz & Meyers (2018), Korb *et al.* (2023), who found that periodic control strategies have a reduced impact on wake behaviour at higher turbulence intensities. Back to floating wind, the computational fluid dynamics (CFD) results from Li *et al.* (2022), Li & Yang (2024) further emphasise the sensitivity of wake dynamics and recovery to varying TI_∞ levels. The findings align with the observations of Yılmaz & Meyers (2018), Korb *et al.* (2023); namely, the effect of rotor motion on wake behaviour decreases relative to that of a fixed turbine as the intensity of the turbulence increases.

From the review of the literature, two key fluid dynamics questions for wind energy remain open: How is wake recovery driven by the large-scale flow structures in the wake of a periodically excited wind turbine and what is the interplay with increasing free-stream turbulence? In this paper we address these questions by means of wind tunnel testings in two facilities (Milan and Oldenburg). We conducted experiments with a model floating wind turbine, varying the rotor motion's amplitude, frequency and direction of motion together with different inflow turbulence intensities ($TI_\infty \in [1.1, 5.8]$ %) modulated by an active grid. Based on the rich literature from previous studies on canonical flows and the wake of fixed wind turbines, we provide an experimental proof of the speculated role of the excited coherent structures on wake recovery. We analyse their development and impact on recovery with different levels of turbulence in the free stream. The paper is organised as follows: § 2 details the experiments used and provides a theoretical basis for the analysis of coherent structures and wake recovery, § 3 presents the results in terms of wake recovery rate budget, recovery with increasing turbulence and motion-induced coherent structures shape and energy depending on the direction and amplitude of motion, § 4 summarises the main findings and § 5 discusses the results, draws parallels with previous work and concludes with their implications for wind energy.

2. Methodology

First, we describe the experimental set-up used for the tests in Milan and Oldenburg and detail the generation and type of inflows considered (§ 2.1). Second, we depict the platform motion cases investigated and wind turbine operating parameters (§ 2.2). Third, we provide a theoretical basis for the analysis of the wake data (§ 2.3).

2.1. *Experimental set-up and inflows*

In this study we carried out complementary measurements in two wind tunnel facilities: Milan (M), Italy (13.8 m × 3.8 m section, length of 35 m) and Oldenburg (O), Germany (3 m × 3 m section, length of 30 m) with a simplified model 'floating' wind turbine. The lab-scale FOWT used is composed of the model wind turbine Oldenburg, MoWiTO 0.6 with a diameter $D = 2R = 0.58$ m mounted on a motorised Stewart platform (see figure 1); further details on the model turbine and platform can be found in Messmer *et al.* (2022, 2024*a*).

In Milan (figure 1*a*) the model turbine was placed 25 m downstream of the inlet. The natural flow of the boundary layer test section is uniform at the rotor area, from bottom tip to top blade tip about 0.67−1.25 m from the ground. The inflow is characterised by a background turbulence intensity $TI_\infty = \sqrt{\overline{u'^2_\infty}}/U_\infty = 1.5 \pm 0.2$ % and an integral length scale of $\mathcal{L}_0/D = 0.2 \pm 0.05$ for $U_\infty = 5$ m s^{-1}, referred to as inflow case M1.5. We computed the integral length scale in the x direction, $\mathcal{L}_0$ as follows: $\mathcal{L}_0 = U_\infty \int_0^{\tau_0} R_{xx}(\tau)\mathrm{d}\tau$ with R_{xx} the auto-correlation function of $u'(t)$ in the free stream and τ_0 the time lag at which $R_{xx}(\tau_0) = 0$ as done by Gambuzza & Ganapathisubramani (2023).

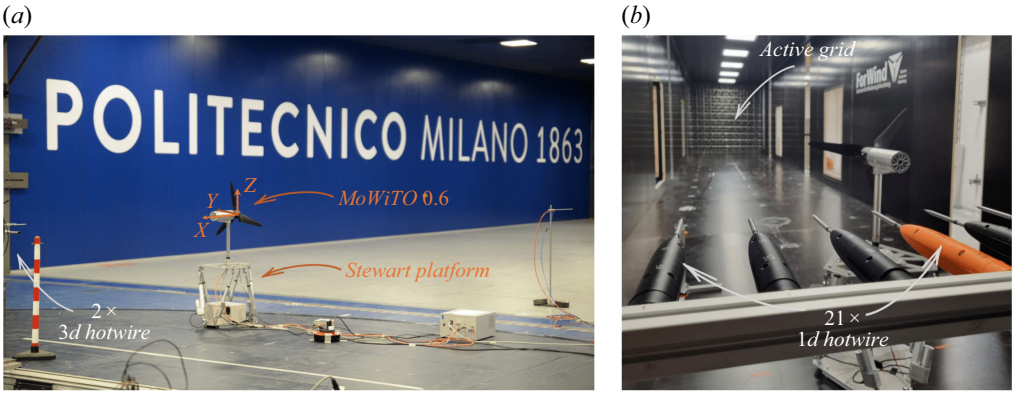

Figure 1. Experimental set-up: MoWiTO 0.6 mounted on the 6-degrees of freedom (DoF) motorised platform. (*a*) Wind tunnel in Milan. (*b*) Wind tunnel in Oldenburg (with active grid).

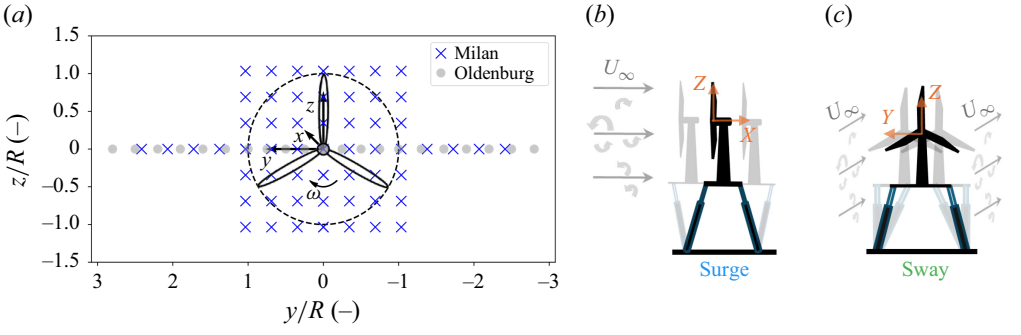

Figure 2. (*a*) Measurement points *y*-*z* positions. (*b*) Picture of surge motion (fore-aft to streamwise). (*c*) Picture of sway motion (sideways to streamwise).

We measured the wake of the wind turbine with two three-dimensional (3-D) hot wires, getting the three components of the wind speed, expressed in a Cartesian frame of reference (see figure 1*a*): $\boldsymbol{u} = u_i \boldsymbol{e_i} = u\boldsymbol{e_x} + v\boldsymbol{e_y} + w\boldsymbol{e_z}$ (with x pointing downstream). The two probes were installed on a motorised mounting that allows translation in the y–z plane and that can be manually moved to different downstream positions, x. With this measurement set-up, we recorded wake data behind the turbine at $x \in \{2, 4, 6, 8, 10\}D$ and different y and z positions (see the blue crosses in figure 2*a*) with a Δy and Δz spacing between points of $0.34R$. Data were recorded with two triaxial fibre-film *Dantec Dynamics 55R91* probes. A temperature correction was applied on the calibration to account for temperature drift, as described in the sensor data sheet (temperature coefficient of resistance, TCR, about 0.5 %/°C). For each point, the measurement lasted 60 s and was sampled with a frequency f_s of 6 kHz. In Milan, three motion cases were investigated; more details are given below.

In Oldenburg (figure 1*b*) the model turbine was placed in the closed test section of the wind tunnel behind an active grid mounted at the inlet. The model was placed at $d_{grid \to turbine} = 10$ m and 15 m downstream of the inlet depending on the inflow cases (see table 1). Such long distances enable the development of a uniform inflow with a low level of turbulence. The active grid used for the experiments is described in more detail in Neuhaus *et al.* (2021). It is composed of 80 independent motorised shafts on which flaps are mounted. Depending on the mean angle of the shaft, $\overline{\alpha}$, rotational speed and the type

Inflow	O1.1	O1.5	M1.5	O1.7	O2.2	O3.0	O4.1	O5.0	O5.8
Wind tunnel	O	O	M	O	O	O	O	O	O
Grid mode	P	P	X	P	P	A	A	A	A
$\overline{\alpha}$ (deg.)	0	10	X	10	25	30	30	30	30
std(α) (deg.)	0	0	X	0	0	5	8.5	11.5	15
$d_{grid->turbine}$(m)	10	15	X	10	10	10	10	10	10
U_∞ (m s^{-1})	3	5	5	3	3	3	3	3	3
$\Delta U_\infty \pm$	0.1	0.1	0.1	0.1	0.1	0.1	0.1	0.1	0.1
TI_∞ (%)	1.1	1.5	1.5	1.7	2.2	3.0	4.1	5.0	5.8
$\Delta TI_\infty \pm$	0.1	0.2	0.2	0.2	0.2	0.2	0.2	0.2	0.2
$\mathcal{L}_0/D$ (−)	0.08	0.2	0.2	0.12	0.2	0.57	1.	1.2	1.2
$\Delta\mathcal{L}_0/D \pm$	0.01	0.05	0.05	0.02	0.05	0.07	0.2	0.2	0.2

Table 1. Inflow cases investigated. Here M stands for Milan and O for Oldenburg.

of shaft motion, the free flow can be tailored to different TI_∞ and $\mathcal{L}_0$. Motivated by real applications for offshore conditions where low to moderate turbulent inflows ($TI_\infty \leqslant 6\,\%$) are found sufficiently frequently to be of relevance (Platis *et al.* 2021; Angelou, Mann & Dubreuil-Boisclair 2023), we investigated cases with $TI_\infty \in\sim [1, 6]\,\%$ and $\mathcal{L}_0 \leqslant 1.2D$. However, in this study we do not analyse and discuss further the role of $\mathcal{L}_0$ on the results.

The active grid was operated in passive mode, noted P (i.e no shaft motion but different mean shaft angles), and active mode, noted A (i.e with shaft motion). For the passive mode, we set a mean angle $\overline{\alpha}$ between 0° and 25°. For the active mode, we used a coupled shaft motion protocol ensuring a constant global blockage of the grid at any time, with a mean shaft angle, $\overline{\alpha}$ of 30° and different levels of fluctuations around the mean, characterised by std(α). We characterised the inflows without the wind turbine model placed by using the same hot-wire array as for the wake measurements, described below. The passive grid modes enabled us to generate inflows with $TI_\infty < 3\,\%$ and the active grid modes, inflows with $TI_\infty \geqslant 3\,\%$. All the inflows analysed in this paper are reported in table 1. Most of the tests were done at U_∞ of 3 m s^{-1} except for the O1.5 case for which $U_\infty = 5$ m s^{-1}, and is a duplicate of the flow from Milan experiments. Important to note is that the inflows generated were far enough from the grid to be fully developed, decaying and in a region where the decay is low so that between $x = 0D$ and $x = 10D$ a maximum of 20 % of decay was observed, meaning that TI_∞ remain sufficiently constant while moving downstream.

We plot in figure 3 the y profile of TI_∞ at hub height (figure 3*a*) and the power spectrum of u'_∞, noted Φ_x of the different inflows with $U_\infty = 3$ m s^{-1} (figure 3*b*). The turbulence within the measurement area is homogeneous (see the low deviation of the different points to the averaged lines in figure 3*a*) with a standard deviation, ΔTI_∞ of maximum 0.2 %. The lowest TI_∞ generated is 1.1 % (case O1.1) with the grid fully open and the highest is 5.8 % (case O5.8) obtained with a large amplitude of shaft motions, characterised by std(α) = 15°. The power spectra in figure 3(*b*) further describe the inflows with regard to the energy distribution across the various flow scales expressed in the frequency domain, fD/U_∞. All inflows feature a typical –5/3 Kolmogorov inertia subrange (Pope 2001), i.e $\Phi_x \propto f^{-5/3}$ for $f \in f_{sub\text{-}range}$ with different ranges depending on the case (see the dashed line in figure 3*b* for the –5/3 slope). Case O1.1, for instance, has the shortest inertia subrange with $f_{sub\text{-}range}D/U_\infty \in\sim [2, 5]$ whereas case O5.8 has the largest with $f_{sub\text{-}range}D/U_\infty \in\sim [0.2, 10]$. Since $\overline{u'^2_\infty} = \int_0^\infty \Phi_x(f)\mathrm{d}f$, the higher TI_∞ cases naturally feature a larger level of energy. Last but not least, whereas passive modes generate inflow

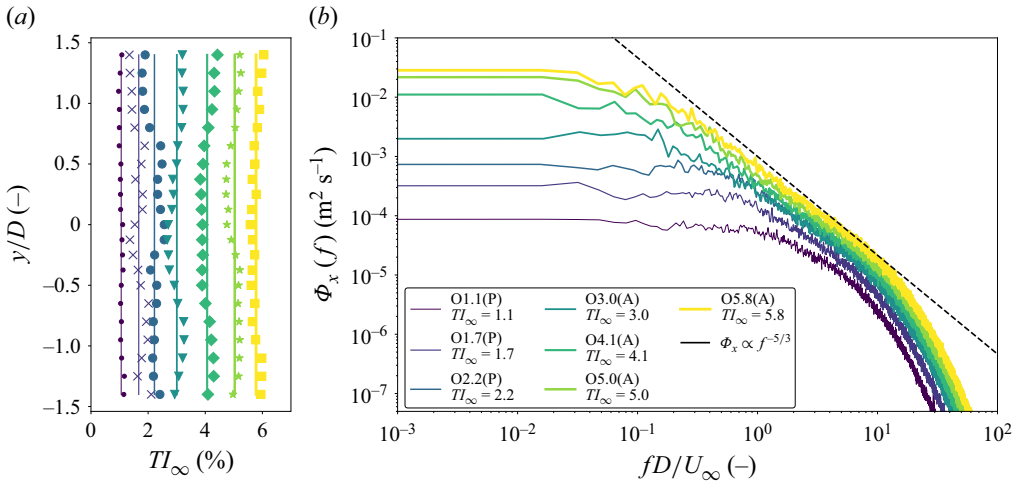

Figure 3. (*a*) Horizontal profile of turbulence intensity at $x = 0D$ (measurement points and mean TI_∞ plotted with solid lines). (*b*) Power spectrum of u'_∞, the turbulent fluctuations of the inflow cases O1.1 to O5.8 in table 1 (with $U_\infty = 3$ m s^{-1}).

with a low level of turbulence intensity and low $\mathcal{L}_0$, active modes lead to larger $\mathcal{L}_0$ up to 1.2D (see table 1).

In Oldenburg the wake measurements were carried out using 21 one-dimensional (1-D) hot wires (grey points in figure 2*a*) aligned horizontally at hub height, measuring a good estimate of u, the streamwise wind speed component. They were mounted on a motorised array enabling them to travel downstream and measure at different x positions. The hot wire covered $y \in [-2.8, 2.8]R$ with a spacing of $\Delta y \approx 0.3R$ and a finer spacing of $\Delta y \approx 0.25R$ within $y \in [-R, R]$. Measurements were taken at $x \in \{2, 4, 6, 8, 10\}D$ for all cases except cases (fixed-5-O, surge-5-O, sway-5-O) hereafter in table 2 for which $x \in [1.5, 10]D$ with $\Delta x = 0.5D$ were measured. Similar to the experiments discussed in Messmer *et al.* (2024*a*), data were acquired with multichannel constant temperature anemometer (54N80-CTA) modules from Dantec Dynamics, with 2-minute measurements per case ($T_{Meas} = 120$ s) and $f_s = 6$ kHz. The hot wires were calibrated twice a day, with a Prandtl tube placed in the free stream as reference for U_∞. Similarly, a Prandtl tube was used to record U_∞ during the wake measurements.

2.2. *Motion cases investigated and turbine parameter*

The review of the literature (§ 1) outlined that rotor excitation, characterised by a Strouhal number $St_a = (f_a D/U_\infty) \approx 0.3$, is often found to be the optimum excitation for wake mixing. Interestingly, when considering realistic motions of floating wind turbines, such as semi-submersibles or spar platforms, the natural period of rotational motion (fore-aft and sideways) often falls within a range of $f_p \approx 1/40$ Hz (Robertson *et al.* 2014). When this frequency is normalised using a typical offshore wind turbine diameter of $D \approx 150$ m and an inflow velocity of $U_\infty \approx 12$ m s^{-1}, it results in a platform Strouhal number, St of ~ 0.3. This suggests that the 'optimum' wake excitation frequency naturally arises in real offshore conditions, reinforcing the relevance of the wake-mixing mechanism for floating wind turbines. The amplitude of platform motion, A_p, varies with environmental conditions but generally remains low, typically below a few degrees (Robertson *et al.* 2014). For small amplitudes ($A_p \leqslant 3°$), we demonstrated in Messmer *et al.* (2024*a*)

Cases	DoF	f_p (Hz)	A_p (mm)	U_∞ (m s^{-1})	St (–)	A^* (–)	Inflows	$x/D \in$
Fixed-5-M	Fixed	0	0	5	0.0	0.0	M1.5	[2, 10], $\Delta x = 2D$
Surge-5-M	Surge	3.33	6	5	0.38	0.01	M1.5	[2, 10], $\Delta x = 2D$
Sway-5-M	Sway	3.33	6	5	0.38	0.01	M1.5	[2, 10], $\Delta x = 2D$
Fixed-5-O	Fixed	0	0	5	0.0	0.0	O1.5	[1.5, 10], $\Delta x = 0.5D$
Surge-5-O	Surge	3.33	6	5	0.38	0.01	O1.5	[1.5, 10], $\Delta x = 0.5D$
Sway-5-O	Sway	3.33	6	5	0.38	0.01	O1.5	[1.5, 10], $\Delta x = 0.5D$
Fixed-3-O	Fixed	0	0	3	0.0	0.0	[O1.1, O5.8]	[2, 10], $\Delta x = 2D$
Surge-3-0.01-O	Surge	1.56	6	3	0.3	0.01	[O1.1, O3.0]	[2, 10], $\Delta x = 2D$
Surge-3-0.017-O	Surge	1.56	10	3	0.3	0.017	[O1.1, O3.0]	[2, 10], $\Delta x = 2D$
Surge-3-0.024-O	Surge	1.56	14	3	0.3	0.024	[O1.1, O5.8]	[2, 10], $\Delta x = 2D$
Sway-3-0.01-O	Sway	1.56	6	3	0.3	0.01	[O1.1, O3.0]	[2, 10], $\Delta x = 2D$
Sway-3-0.017-O	Sway	1.56	10	3	0.3	0.017	[O1.1, O5.0]	[2, 10], $\Delta x = 2D$
Sway-3-0.024-O	Sway	1.56	14	3	0.3	0.024	[O1.1, O5.8]	[2, 10], $\Delta x = 2D$

Table 2. Matrix of motion cases and inflows. Here DoF stands for degree of freedom.

that rotational motions are equivalent to translational ones in terms of wake behaviour. Therefore, in this study we focus on single translational surge (fore-aft) and sway (sideways) motions. Figures 2(*b*) and 2(*c*) illustrate surge and sway motions, respectively. We consider idealised harmonic motion, characterised by a single reduced amplitude, $A^* = A_p/D$, and Strouhal, St, giving a motion signal, $\xi(t)$:

$$\xi(t) = A^* D \sin\left(2\pi\left(\frac{St U_\infty}{D}\right)t\right). \tag{2.1}$$

In Milan we measured the wake for three motion cases: fixed turbine ($St = 0$, used as reference), and surge and sway motions with $St = 0.38$, $A^* = 0.01$, with a free-stream velocity of $U_\infty = 5$ m s^{-1}. As concluded by Yılmaz & Meyers (2018), a rotor excitation frequency corresponding to $St = 0.38$ is effective for enhancing wake mixing, providing further motivation for the selected cases. The turbine was operated with a constant blade pitch and a tip speed ratio of $\lambda = (R\omega/U_\infty) = 6 \pm 0.1$ (ω is the rotor rotational speed), close to the turbine optimum. The thrust coefficient was measured using a strain gauge mounted at the bottom of the tower, yielding $\overline{C_T} = 0.86 \pm 0.05$. These tests are referred to as fixed-5-M, surge-5-M and sway-5-M in table 2.

In Oldenburg we repeated the same motion cases as in Milan under equivalent inflow conditions using the active grid to reproduce the free-stream turbulence ($TI_\infty = 1.5$ %), and maintained the same turbine operating parameters.

In addition, we conducted further tests with $St = 0.3$ – identified in the literature as optimal for wake mixing – with three low motion amplitudes: $A^* \in \{0.01, 0.017, 0.024\}$, with a wind speed U_∞ of 3 m s^{-1}. The choice of lower inflow velocity enabled the testing of higher A^* values (bounded by the platform's maximum physical amplitude A_p at a given motion frequency f_p, as discussed in Messmer *et al.* (2022)) while preserving comparable wake dynamics and recovery behaviour, as shown in Messmer *et al.* (2024*a*). This is explained by the sufficiently high Reynolds number, $Re = DU_\infty/\nu = 1.4 \times 10^5$ (for $U_\infty = 3$ m s^{-1}), which ensures that the wake behaviour is independent of Re for $U_\infty \geqslant 3$ m s^{-1}.

For the $St = 0.3$ cases, we varied the inflow turbulence intensity, TI_∞, from 1.1 % (case O1.1) to 5.8 % (case O5.8), to explore the combined effects of motion and turbulence on

wake behaviour. The turbine was also operated at $\lambda = 6 \pm 0.1$, and we measured a thrust coefficient of $\overline{C_T} = 0.80 \pm 0.05$. All investigated cases are summarised in table 2.

In Kleine *et al.* (2022) the authors analysed the effect of platform motion on the interaction between blade-tip flow structures and platform motion. They define the ratio between the platform motion frequency, f_p, and the rotor rotational frequency, $\omega/2\pi$, as $\omega^* = (2\pi f_p/\omega) = (\pi St/\lambda)$. In our experiments, since $\lambda = 6$, we have $\omega^* \in \{0.16, 0.2\}$ for $St \in \{0.3, 0.38\}$. This indicates that the platform motion's frequency is about five times slower than the rotor rotation frequency and lies below the range where the strongest interaction between motion and vortex structures in the near wake is expected, as described in Kleine *et al.* (2022), namely $\omega^* \in \{0.5, 1.5\}$.

The data collected in the two wind tunnels are complementary. The experiments conducted in Milan provide 3-D wake measurements, which are crucial for assessing the role of coherent structures in wake recovery mechanisms as depicted later on. However, these measurements are limited to a smaller set of motion and inflow conditions, as well as fewer downstream positions.

In contrast, the Oldenburg experiments offer 1-D wake field data at a greater number of downstream positions than those available from the Milan tests, for the three shared cases (fixed-5, surge-5, sway-5). This extended spatial coverage is essential for computing streamwise gradient terms (e.g. $\partial/\partial x$). Additionally, the Oldenburg data include a wider range of motion and inflow conditions, with simultaneous measurements enabling the reconstruction of the motion-induced large-scale wake structures.

2.3. *Mathematical concepts on wake recovery and coherent structures*

In this work we are interested in wake recovery as defined in Boudreau & Dumas (2017), i.e the average wind speed in the wake on the rotor area. Since we mainly measure on a horizontal line at hub height, we define the recovery as

$$R_w(x) = \int_{y_c-R}^{y_c+R} \overline{u(x, y, t)} \mathrm{d}y/(DU_\infty) = \langle \overline{u} \rangle / U_\infty, \quad \text{for} \quad y_c \approx 0, \tag{2.2}$$

where y_c is the wake centre identified as the region where $\overline{u}$ is the lowest, in this paper for most cases $y_c \approx 0$. Here $\langle \cdot \rangle$ is the integrated value in the rotor area normalised by D; R_w provides a good estimate of the wind available for a potential downstream wind turbine aligned with the one upfront generating the wake. The rate, $\partial R_w/\partial x$, at which the wake recovers can be expressed directly by the Reynolds-averaged Navier–Stokes equation (RANS), as done for a fixed wind turbine by Bastankhah & Porté-Agel (2016), Boudreau & Dumas (2017), van der Laan, Baungaard & Kelly (2023). The local RANS equation projected in $\boldsymbol{e_x}$ gives

$$\frac{D}{U_\infty}\frac{\partial \overline{u}}{\partial x} = -\frac{D}{U_\infty}\frac{1}{\overline{u}}\left[\frac{1}{\rho}\frac{\partial \overline{p}}{\partial x} + \overline{v}\frac{\partial \overline{u}}{\partial y} + \overline{w}\frac{\partial \overline{u}}{\partial z} + \frac{\partial \overline{u'u'}}{\partial x} + \frac{\partial \overline{u'v'}}{\partial y} + \frac{\partial \overline{u'w'}}{\partial z}\right] \tag{2.3}$$

after Boudreau & Dumas (2017), we neglected the viscous term $1/Re \cdot \nabla^2 \boldsymbol{u_i} \cdot \boldsymbol{e_x}$ since $Re \gg 1$. The integration of (2.3) provides a decomposition of the contribution of the different terms to wake recovery. In this paper and based on our previous work (Messmer *et al.* 2024*a*), we investigate platform motion cases that lead to the formation of a synchronised coherent structure at the motion frequency characterised by St. In such cases, the wake flow field can be decomposed as (Reynolds & Hussain 1972; Baj, Bruce & Buxton 2015; Lignarolo *et al.* 2015)

$$u_i = \overline{u_i} + u_i' = \overline{u_i} + \widetilde{u_i} + u_i'', \tag{2.4}$$

where the velocity fluctuations u_i' are split up into $\widetilde{u_i}$, the contribution from the coherent structure of St (with a frequency f_p) and u_i'', the stochastic turbulent contribution, i.e the velocity fluctuations without any periodic coherence. As done in Cantwell & Coles (1983), $\widetilde{u_i}$ is calculated by phase averaging the measured wind speed signals so that $\widetilde{u_i}(\phi(t)) = \widetilde{u_i}(\phi(t + 1/f_p))$. Here, $\phi(t)$ is the instantaneous phase of the periodic wake motion, typically defined based on the known excitation frequency f_p,

$$\phi(t) = 2\pi f_p t + \phi_0, \tag{2.5}$$

where ϕ_0 denotes the initial random phase shift. Throughout this paper, we use the normalised phase defined as $\phi^* = (\phi(t) - \phi_0) \bmod 2\pi$, which maps the phase into a dimensionless range $\phi^* \in [0, 2\pi]$. Further details on the methodology used to compute $\widetilde{u_i}$ are provided in Appendix A. Per definition, $\overline{\widetilde{u_i} u_i''} = 0$. Accounting for the decomposition of (2.4) in (2.3) writes as

$$\frac{D}{U_\infty}\frac{\partial \overline{u}}{\partial x} = -\frac{D}{U_\infty}\frac{1}{\overline{u}}\left[\frac{1}{\rho}\frac{\partial \overline{p}}{\partial x} + \overline{v}\frac{\partial \overline{u}}{\partial y} + \overline{w}\frac{\partial \overline{u}}{\partial z} + \frac{\partial \overline{u''u''}}{\partial x} + \frac{\partial \overline{\widetilde{u}\widetilde{u}}}{\partial x} + \frac{\partial \overline{u''v''}}{\partial y} + \frac{\partial \overline{\widetilde{u}\widetilde{v}}}{\partial y} + \frac{\partial \overline{u''w''}}{\partial z} + \frac{\partial \overline{\widetilde{u}\widetilde{w}}}{\partial z}\right]. \tag{2.6}$$

The recovery rate $D\partial R_w/\partial x := D/U_\infty \langle \partial \overline{u}/\partial x \rangle$ is obtained from (2.6) by spatial integration of each term as done in (2.2). The recovery rate budget, i.e. the different physical mechanisms that contribute to the restoration of the mean flow velocity in the wake, is composed of the following terms.

(i) The mean pressure gradient ($-\partial \overline{p}/\partial x < 0$): the turbine induces a large pressure drop that restores primarily to momentum (Boudreau & Dumas 2017). This term can thus be viewed as a sink for the 'recovery' process.

(ii) The mean speed transverse transport terms ($-\overline{v}\partial \overline{u}/\partial y$ and $-\overline{w}\partial \overline{u}/\partial z$): wake rotation generates horizontal and vertical mean wind speed components, $\overline{v}$ and $\overline{w}$, involved in momentum transport (Boudreau & Dumas 2017).

(iii) The gradient of the Reynolds shear stress terms from incoherent fluctuations ($-\partial \overline{u''v''}/\partial y$ etc.): incoherent turbulent fluctuations transport momentum and are the primary contributors to wake recovery (van der Laan *et al.* 2023; Gambuzza & Ganapathisubramani 2023).

(iv) The gradient of the Reynolds shear stress terms from the coherent fluctuations ($-\partial \overline{\widetilde{u}\widetilde{v}}/\partial y$ etc.): the organised structures may also contribute to wake recovery, though their role has not been extensively studied in previous research on wind turbine wakes, and is therefore addressed in this paper.

3. Results

First, in § 3.1 we present results from the shared cases between Milan and Oldenburg at $TI_\infty = 1.5\,\%$ (M1.5 and O1.5 inflow cases in table 1). Using these detailed datasets, we compute the terms of the recovery rate budget (2.6) and provide quantitative evidence for the role of coherent structures in enhancing wake recovery. Second, in § 3.2 we show how wake profiles and recovery vary with inflow turbulence intensity and platform motion amplitude, at a fixed Strouhal number of $St = 0.3$. Third, § 3.3 focuses on the coherent structures formed in the wake. We analyse their shape, strength and dependence on both TI_∞ and the type of rotor motion. Fourth, based on these structures, § 3.4 explores their

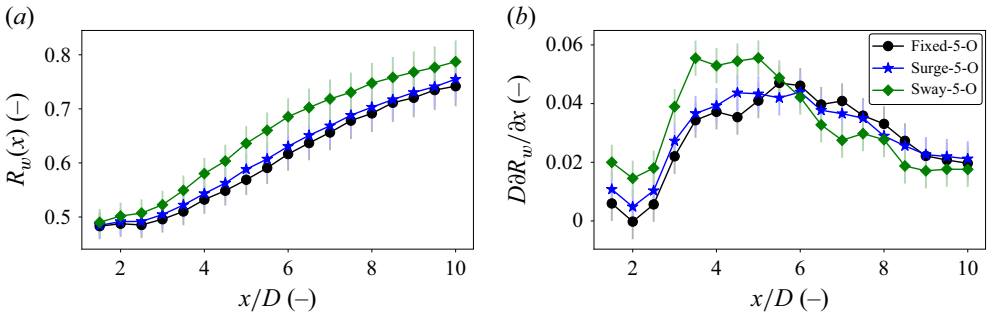

Figure 4. (*a*) Wake recovery (2.2) for the fixed-5-O, surge-5-O and sway-5-O cases ($St = 0.38$, $A^* = 0.01$). Error bars represent the average discrepancy between the Milan and Oldenburg datasets (Appendix B). (*b*) Wake recovery rate. Error bars represent the estimated uncertainty based on a Monte Carlo approach (Appendix B). Both quantities are derived from the Oldenburg dataset.

influence on phase-resolved wake recovery. Finally, § 3.5 examines the energy content of the coherent structures and analyses the dependency on inflow turbulence and platform motion energy and relation with increased recovery compared with the fixed case.

3.1. *Wake recovery mechanisms*

We begin the results section by presenting findings from the shared cases of the Milan and Oldenburg experiments. In Appendix B we detail the close agreement between the two datasets, as well as the methodology used to compute the various terms of (2.6), which supports the combined use of both datasets. The 3-D wake fields from Milan enable the computation of the $\partial/\partial y$ and $\partial/\partial z$ terms, while the 1-D measurements from Oldenburg, with their higher resolution in the streamwise direction, are used to compute the $\partial/\partial x$ terms. Details regarding the estimation of uncertainty in the derivative calculations are also provided in Appendix B.

For the three shared motion cases (fixed-5, surge-5 and sway-5; see table 2), figure 4(*a*) shows the evolution of wake recovery and figure 4(*b*) presents the normalised recovery rate, $D\partial R_w/\partial x$. The wake of the moving turbine recovers more rapidly – with approximately 14 % higher recovery for the sway case and 3 % for surge compared with the fixed case at $x = 6D$. Correspondingly, the recovery rate (figure 4*b*) is higher for both sway and surge motions up to $x \leqslant 5D$. This enhancement in wake recovery is less pronounced than in cases with laminar inflow, as reported by Li *et al.* (2022) and Messmer *et al.* (2024*a*). Compared with surge motion, sway leads to a 11 % higher recovery, even though both cases share the same values of St and A^*. This result provides an initial indication that sway motion has a larger impact on wake recovery enhancement than surge motion – a point we investigate in more detail later in § 3.2.

In the following, we examine the mechanisms behind the enhanced wake recovery found with rotor motion. Figure 5 presents horizontal (y) profiles of the individual terms in the recovery rate budget. At $x = 4D$ (figure 5*a–c*), the black dotted line highlights a larger value of $\partial\overline{u}/\partial x$ for the sway case (figure 5*c*) compared with the fixed case (figure 5*a*), particularly within $y \in [-0.5D, 0.5D]$. While the fixed and surge cases still exhibit characteristics of a developing wake – evidenced by a double-Gaussian-like shape in $\partial\overline{u}/\partial x$ – the sway case presents a developed wake profile, already resembling the single-Gaussian distribution typical of the far wake (Neunaber *et al.* 2020). This suggests that sway motion promotes a faster transition to the far-wake regime. By $x = 8D$ (figure 5*d–f*), all cases display Gaussian-like $\partial\overline{u}/\partial x$ profiles, confirming that the far wake has been

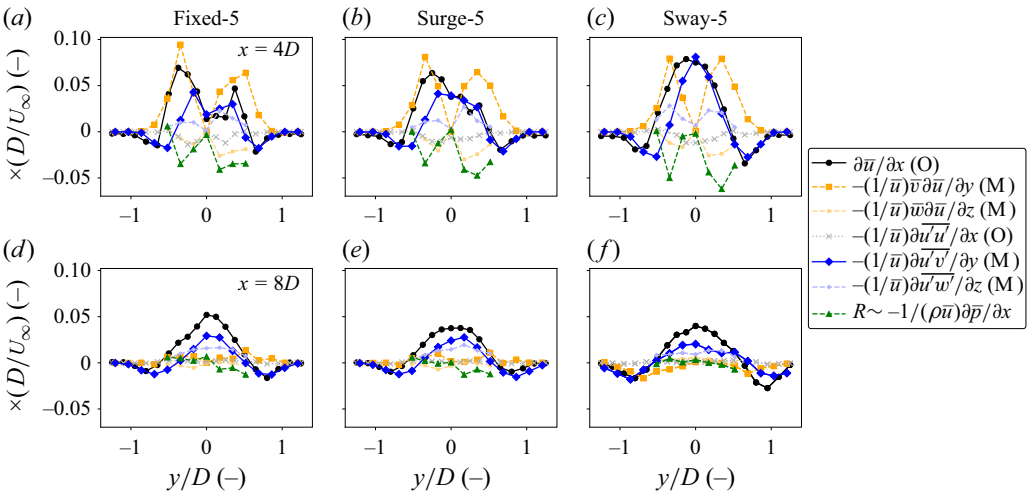

Figure 5. The y profiles of the terms in the recovery rate budget (2.6) for the fixed-5 (a,d), surge-5 (b,e) and sway-5 (c,f) cases. Panels (a–c) correspond to $x = 4D$ and panels (d–f) to $x = 8D$. In the legend, (M) indicates terms computed using Milan data, while (O) indicates those based on Oldenburg data.

reached for all cases. These findings are consistent with observations under laminar inflow conditions reported by Messmer *et al.* (2024*a*), where platform motion was shown to accelerate wake development.

Returning to the profiles at $x = 4D$, the primary contributor to the positive $\partial\overline{u}/\partial x$ appears to be the term $-(1/\overline{u})\partial\overline{u'v'}/\partial y$, i.e. the gradient of Reynolds shear stress in the x–y plane. The gradient of $u'w'$ (the x–z component) also contributes positively to wake recovery. As discussed in Boudreau & Dumas (2017), van der Laan *et al.* (2023), Gambuzza & Ganapathisubramani (2023), these terms are known to dominate wake recovery processes. The negative regions of $\partial\overline{u}/\partial x$ observed at the edges of the wake ($|y| > 0.5D$) act as sinks of recovery, supplying momentum toward the wake centre where $\partial\overline{u}/\partial x > 0$, consistent with the interpretation of van der Laan *et al.* (2023). The y-rotational term, $-(1/\overline{u})\overline{v}\partial\overline{u}/\partial y$, is positive and, thus, contributes mathematically to $\partial\overline{u}/\partial x > 0$; whereas the other rotational term, $-(1/\overline{u})\overline{w}\partial\overline{u}/\partial z$ is negative. The sum of the two appears to be counterbalanced by the remaining residual, which is mathematically equivalent to the pressure gradient term. Finally, figure 5(*d*–*f*) shows that at $x = 8D$ the recovery rate is higher for the fixed case (figure 5*d*) than for the sway case (figure 5*f*), in agreement with the results shown previously in figure 4(*b*). At this downstream location, all cases have transitioned to the far-wake regime, where recovery is primarily driven by gradients in Reynolds shear stresses in both the x–y and x–z planes.

To provide a broader view, we integrate all terms of the recovery rate budget (2.6) over the rotor diameter, following the same approach used in (2.2) for $\overline{u}$. This integration yields a quantitative assessment of each term's contribution (rotation, pressure, Reynolds stresses) to the overall recovery rate. Figure 6 presents the downstream evolution of these integrated contributions. Sway motion leads to a substantial increase in the Reynolds stress gradient terms in both the streamwise – spanwise and streamwise–vertical planes – up to 65 % higher than in the fixed case (blue ♦ symbols in figure 6(*a*,*c*). In contrast, surge motion shows only a modest enhancement of these terms. Meanwhile, mean flow transport terms (associated with $\overline{v}$ and $\overline{w}$) decay more rapidly for sway – see the yellow ■ symbols at $x = 6D$ in figure 6(*c*) – compared with fixed and surge cases. The turbulent transport in the x direction (grey ×) acts as a mild sink of recovery in all cases.

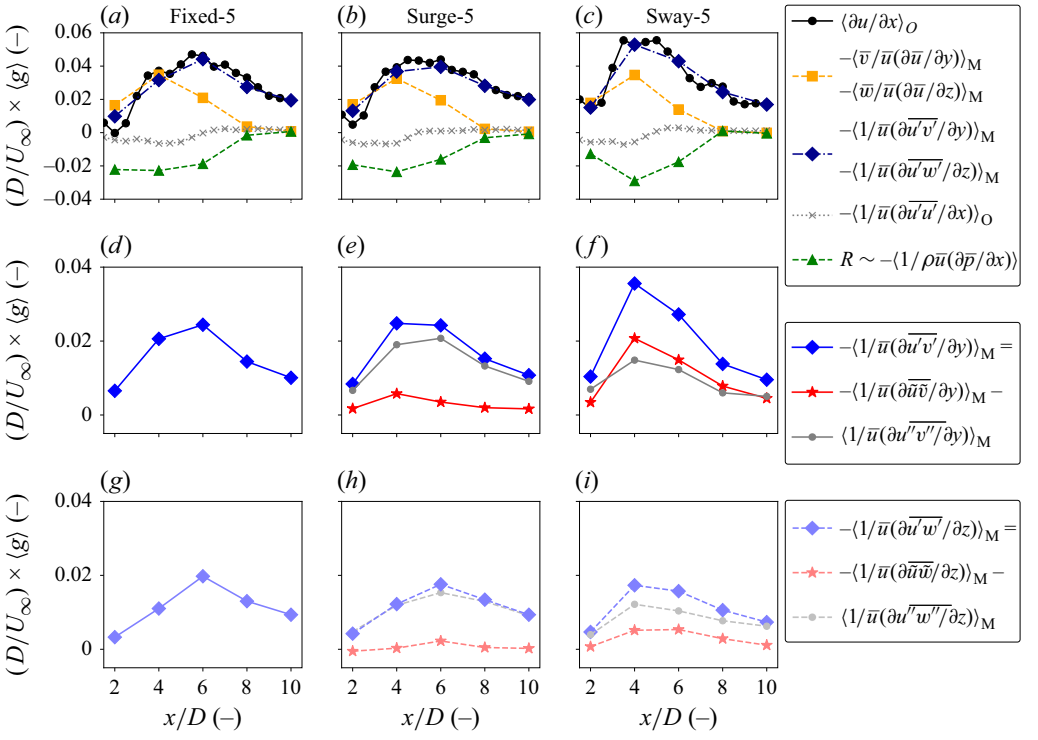

Figure 6. Downstream evolution of recovery equation terms (2.6) integrated over the rotor diameter for fixed-5 (*a*), surge-5 (*b*) and sway-5 (*c*). Panels (*d–f*) show x–y Reynolds shear stress gradients; panels (*g–i*) show x–z gradients for the same cases.

Notably, the residual term (green ▲) emerges as the dominant sink, suggesting that a large portion of the momentum rate budget is associated with pressure restoration or rotation-induced pressure effects. Noriega & Mazellier (2025) showed, using a porous disk with tilted blades, that wake rotation can induce a low-pressure core in the wake. This low-pressure region likely counteracts the potential benefits of rotational effects on wake recovery. In fact, between $x = 4D$ and $8D$, the rotation contribution (yellow ■) appears nearly balanced by the residual, potentially indicating a negligible net impact on recovery.

Most importantly, for $x \in [2D, 6D)$, the enhanced recovery observed for sway primarily originates from the increased Reynolds stress gradient terms: $-\langle (1/\overline{u})\partial \overline{u'u'_i}/\partial x_i \rangle$ with $i \in y, z$. These terms represent turbulent transport in the x–y and x–z planes, and have been consistently identified as key contributors to wake recovery in previous studies on fixed wind turbines (Bastankhah & Porté-Agel 2016; Boudreau & Dumas 2017; Gambuzza & Ganapathisubramani 2023; van der Laan *et al.* 2023). Finally, for $x \gtrsim 8D$, the far-wake regime is reached, where the recovery rate $D\partial R_w/\partial x$ is well approximated by the combined Reynolds shear stress gradients, i.e. $D\partial R_w/\partial x \approx -\langle (1/\overline{u})(\partial \overline{u'v'}/\partial y + \partial \overline{u'w'}/\partial z) \rangle$ where rotation and pressure terms are zero (Gambuzza & Ganapathisubramani 2023).

For a clearer insight into the underlying processes, we next explore the decomposition of the Reynolds shear stresses. In the $x-y$ plane the total term is expressed as $-\langle 1/\overline{u}\partial \overline{u'v'}/\partial y \rangle = -\langle 1/\overline{u}\partial \overline{\tilde{u}\tilde{v}}/\partial y \rangle - \langle 1/\overline{u}\partial \overline{u''v''}/\partial y \rangle$ (see figure 6*d–f*) and in the $x-z$ plane it is written as $-\langle 1/\overline{u}\partial \overline{u'w'}/\partial z \rangle = -\langle 1/\overline{u}\partial \overline{\tilde{u}\tilde{w}}/\partial z \rangle - \langle 1/\overline{u}\partial \overline{u''w''}/\partial z \rangle$

(see figure 6*g–i*). Here, the tilde terms $\widetilde{\overline{uv}}$ and $\widetilde{\overline{uw}}$ represent the contributions from the coherent structures induced by platform motion at a given St, while the double-prime terms $\overline{u''v''}$ and $\overline{u''w''}$ capture the contributions from purely stochastic turbulence.

Figure 6(f) shows that the total gradient of the Reynolds shear stress in the $x-y$ plane is significantly enhanced for the sway case compared with the fixed case (compare the blue ♦ symbols in figures 6*d* and 6*f*). Surprisingly, for sway and $3D \lesssim x \lesssim 10D$, more than half of the total $x-y$ term is covered by $\langle 1/\overline{u}\partial\widetilde{\overline{uv}}/\partial y\rangle$, i.e the coherent structure contribution. In contrast, the $x-z$ plane (figure 6*i*) shows both a lower overall Reynolds shear stress gradient and a relatively smaller contribution from the coherent structure subterm. Although surge motion (figures 6*e* and 6*h*) also exhibits contributions from coherent structures in both the $x-y$ and $x-z$ planes, these are much lower than those observed for sway, reflecting its reduced impact on wake recovery.

These results conclusively show that the coherent structures induced by platform motion play a critical role in enhancing wake recovery. Consistent with previous findings on fixed wind turbines (Boudreau & Dumas 2017; van der Laan *et al.* 2023), our study shows that the gradients of Reynolds shear stress in the $x-y$ and $x-z$ planes are central to the recovery process. In the sway case, the improved recovery – evidenced by the higher $D\partial R_w/\partial x$ in figure 4(a) – is directly linked to increased Reynolds stress gradient terms: $-\langle 1/\overline{u}\partial\overline{u'v'}/\partial y\rangle - \langle 1/\overline{u}\partial\overline{u'w'}/\partial z\rangle$.

Notably, a substantial portion of these gradients is attributable to the contributions of coherent structures – an observation that supports our earlier speculation in Messmer *et al.* (2024*a*). Previous studies, such as Yılmaz & Meyers (2018), Korb *et al.* (2023), Van der Hoek *et al.* (2024), have similarly linked the presence of coherent structures from periodic excitations to mechanisms like wake deflection and enhanced momentum entrainment. In our work, the effect of these mechanisms on recovery are quantitatively represented by the two terms: $-\langle 1/\overline{u}\partial\widetilde{\overline{uv}}/\partial y\rangle - \langle 1/\overline{u}\partial\widetilde{\overline{uw}}/\partial z\rangle$.

Later in the paper we further decompose wake recovery by distinguishing the effects of periodic wake deflection and enhanced momentum entrainment, both of which are influenced by periodic structures, as discussed in Korb *et al.* (2023). These factors are, to some extent, hidden in our recovery rate budget analysis.

3.2. *Wake profiles and recovery with increasing free-stream turbulence*

So far, we have investigated wake recovery for a specific inflow condition with $TI_\infty = 1.5\,\%$ and fixed values of St and A^*. Next, we present the results on wake profiles and recovery for a range of inflows with different TI_∞ (O1.1−O5.8 in table 1) and for various motion cases with $St = 0.3$ and $A^* \in \{0.01, 0.017, 0.024\}$ (see table 2). As detailed in § 2.1, the active grid at the University of Oldenburg was used to achieve TI_∞ levels in the range $[1.1, 5.8]\,\%$. These experiments allow us to assess the combined effects of increasing inflow turbulence and platform motion on wake development and recovery.

We present in figure 7 the lateral (y) profiles of the normalised wake deficit $\Delta u^* = (U_\infty - \overline{u})/U_\infty$ (figure 7*a*) and turbulence intensity $TI = \sqrt{\overline{u'^2}}/\overline{u}$ (figure 7*b*). The data are organised as follows.

(i) Three inflow conditions, with $TI_\infty \in \{1.1, 3.0, 5.8\}\,\%$, corresponding to cases O1.1, O3.0 and O5.8 from table 1), shown respectively in (a–0)–(a–4), (b–0)–(b–4), (c–0)–(c–4).
(ii) Two motion amplitudes per motion type ($A^* = 0.01,\ 0.024$) for both surge and sway, with $St = 0.3$.
(iii) Five downstream locations, $x \in [2,\ 10]D$ denoted (.–0)–(.–4), where '.' stands for a, b or c.

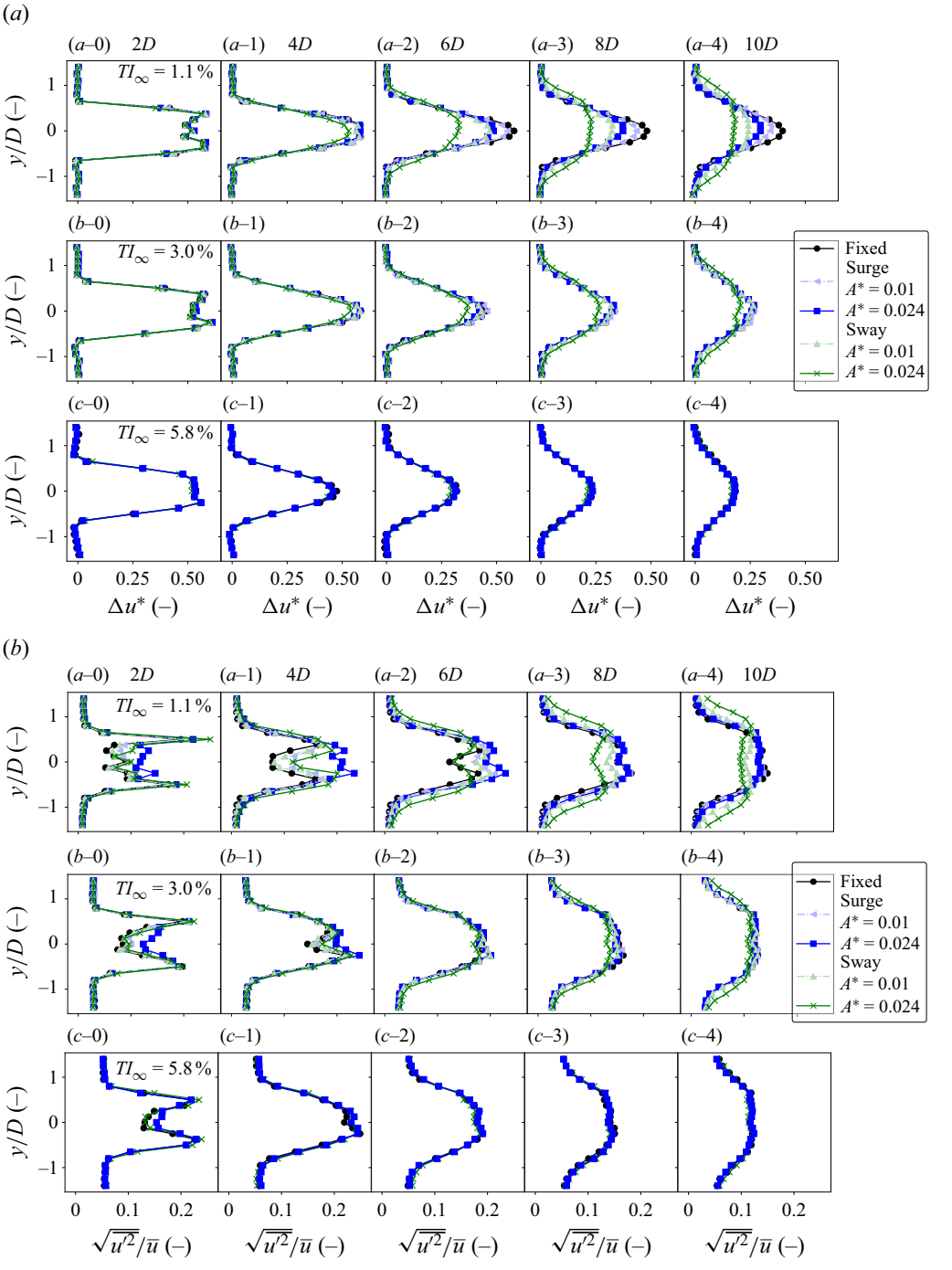

Figure 7. The y profiles of normalised wake deficit (a) and turbulence intensity (b) for fixed, surge- and sway-3–0.01 and 0.024, i.e $St = 0.3$, $A^* = 0.01,\ 0.024$ (see table 2) for O1.1 (a–0)–(a–4), O3.0 (b–0)–(b–4), O5.8 (c–0)–(c–4) and $x \in [2,\ 10]D$ (0,4). Inflows in table 1.

Figure 7(*a*) (*a*–0), (*b*–0) and (*c*–0) reveal that, in the near wake at $x = 2D$, the wake deficit profiles are nearly identical across all motion cases for a given inflow condition. This observation, consistent with earlier findings by Fontanella, Zasso & Belloli (2022) and Messmer *et al.* (2024*a*) (in low turbulent inflows, $TI_\infty < 2\,\%$), suggests that the mean induction, i.e. the average slowing of the flow by the turbine, is effectively unchanged between cases. In other words, $\overline{C_T}$ is constant across motion cases. This equivalence is crucial as it ensures that any observed differences in wake evolution further downstream can be attributed to platform motion effects rather than discrepancies in the initial near-wake, rotor-induction conditions.

As we move downstream, figure 7(*a*) (*a*–0)–(*a*–4) illustrate the pronounced impact of platform motion on the wake deficit under low inflow turbulence ($TI_\infty = 1.1\,\%$). Both surge and sway cases show enhanced wake recovery relative to the fixed case, with the most significant effect observed for sway motion at the highest amplitude ($A^* = 0.024$, green $\times$). This case produces a much broader and more uniform velocity deficit profile compared with the fixed case (black dots), indicating that sway motion promotes a wider wake and accelerates lateral wake expansion. Notably, by $x = 10D$, the wake profile for this sway case deviates from the classic Gaussian shape, potentially challenging conventional analytical wake models (e.g. the Bastankhah & Porté-Agel (2014) wake model). In contrast, the lower amplitude case (green triangle) yields a wake profile more similar to the fixed case, suggesting a weaker influence on wake growth. Comparing the two motion directions, sway induces more noticeable changes in the wake mean structure than surge, which remains closer to the fixed reference across all downstream positions.

As inflow turbulence increases, the influence of motion diminishes. At $TI_\infty = 3.0\,\%$, the sway-induced differences are still visible (figure 7*a* (*b*–2)–(*b*–4)), but to a lesser extent. For surge motion, however, this turbulence level appears to mark a threshold – no discernible difference is observed between the surge and fixed cases, even at the highest motion amplitude. Finally, under higher turbulence ($TI_\infty = 5.8\,\%$), all wake deficit profiles converge, indicating that inflow turbulence dominates the wake mean profiles and suppresses any motion-induced effects.

Concordantly, the differences in the turbulence intensity profiles between the motion cases and the fixed case are most pronounced under low inflow turbulence ($TI_\infty = 1.1\,\%$), as shown in figure 7(*b*) (*a*–0)–(*a*–4).

Surge motion primarily increases the level of turbulence intensity within the rotor region ($|y| < 0.5D$); for instance, at $x = 4D$, the surge case with $A^* = 0.024$ (blue squares) shows a pronounced increase in turbulence intensity compared with the fixed case (black dots), as seen in figure 7(*b*) (*a*–1). This elevated turbulence accelerates the transition to the far-wake regime, as detailed in Messmer *et al.* (2024*a*). The influence of motion amplitude is clear: the lower amplitude case ($A^* = 0.01$) induces only a slight increase in turbulence intensity, consistent with its weaker effect on the wake deficit seen in figure 7(*a*) (*a*–0)–(*a*–4).

Sway motion, by contrast, predominantly enhances turbulence intensity at the edges of the wake ($|y| > 0.5D$), particularly at downstream locations ($x \in [8D, 10D]$); see green crosses in figures 7(*b*) (*a*–3) and 7(*b*) (*a*–4). Similar to the trends observed for Δu^*, lateral platform motion results in a broader and more uniform turbulence intensity distribution, with a lower intensity in the wake centre and a higher intensity at the edges – indicating a wider and more dispersed wake for the larger amplitude sway case.

As TI_∞ increases, the influence of platform motion on wake turbulence intensity diminishes. At $TI_\infty = 3.0\,\%$, surge motion with $A^* = 0.024$ leads to a moderate increase in near-wake turbulence for $x \leqslant 4D$ (figure 7*b* (*b*-0)–(*b*-1)). Sway motion at this turbulence level still causes slight wake broadening in the far wake ($x \geqslant 8D$), though the effect is noticeably reduced compared with the lower TI_∞ case (figure 7*b* (*b*–3)–(*b*–4)). For both

surge and sway, the lower amplitude case ($A^* = 0.01$) shows no discernible effect on turbulence intensity profiles when $TI_\infty \geqslant 3\,\%$.

Finally, at the highest inflow turbulence ($TI_\infty = 5.8\,\%$), platform motion has negligible impact on turbulence intensity across all downstream positions beyond $x = 2D$ (figure 7*b* (*c*–1)–(*c*–4)).

This analysis of the turbulence intensity profiles, in agreement with the wake deficit observations, confirms that the effect of platform motion weakens as inflow turbulence increases. This trend aligns well with previous CFD studies by Yılmaz & Meyers (2018) and Li *et al.* (2022).

We next quantify the differences between the fixed case and the motion cases for multiple inflow turbulence levels TI_∞ and all amplitudes of motion. To do so, we compute the recovery using (2.2) for the fixed case ($St = 0$), as well as for surge and sway motions at $St = 0.3$ with $A^* \in \{0.01, 0.017, 0.024\}$ (table 2). Figure 8(*a–f*) shows the results for the different inflow turbulence conditions $TI_\infty \in \{1.1, 2.2, 3.0, 4.1, 5.0, 5.8\}\ \%$.

As noted earlier in the wake deficit profiles (figure 7*a*), for a given inflow condition, all cases – fixed or with platform motion – exhibit nearly identical wake recovery at $x = 2D$. The effect of platform motion on the wake develops progressively farther downstream, driven by nonlinear interactions (Messmer *et al.* 2024*a*). Between the different inflow cases, $R_w(x = 2D)$ varies slightly but remains close to $R_w \approx 0.5$.

The clearest differences between motion cases appear for the lowest free-stream turbulence level $TI_\infty = 1.1\ \%$ (figure 8*a*), consistent with the wake profiles in figure 7(*a*). Sway motion with $A^* = 0.024$ improves recovery by up to 21 % compared with the fixed case. For both surge and sway, the impact is less with decreasing motion amplitude; for example, sway with $A^* = 0.01$ yields a 12 % increase in recovery over the fixed case. Interestingly, even the largest surge amplitude results in a weaker recovery enhancement than sway motion at the lowest amplitude.

As TI_∞ increases (figure 8*b–f*), the influence of platform motion diminishes. At $TI_\infty = 2.2\ \%$ (figure 8*b*), surge with $A^* = 0.024$ enhances recovery by only 3.5 %, while sway still yields an 11 % increase. Sway at $A^* = 0.01$ continues to improve recovery by 4 %, whereas surge at the same amplitude has no observable effect. At $TI_\infty = 3.0\ \%$ (figure 8*c*), surge and fixed recovery curves overlap entirely, while sway continues to provide a 5 % improvement. The effect of sway becomes almost negligible around $TI_\infty = 5.0\ \%$, and at $TI_\infty = 5.8\ \%$ all cases, fixed, surge and sway, converge.

Figure 8 highlights three important trends. First, sway motion has a stronger influence on wake recovery than surge, a result we further quantify and discuss later in this paper. Second, larger motion amplitudes lead to greater recovery improvements, as also pointed out by Li *et al.* (2022), Messmer *et al.* (2024*a*). Third, the effect of platform motion does not add linearly to the effect of inflow turbulence; rather, the two blend. To highlight this point, we present in figure 9 the downstream evolution of offset-adjusted wake recovery, denoted as R_w^*, for the fixed case (figure 9*a*) and for the sway case with $A^* = 0.024$ (figure 9*b*), across all levels of inflow turbulence, $TI_\infty \in [1.1, 5.8]\ \%$.

We define the adjusted recovery as

$$R_w^*(x) = R_w(x) - R_w(x = 2D) + 0.5 \tag{3.1}$$

in order to align all curves at a common starting point of 0.5 at $x = 2D$, thereby removing small variations in $R_w(x = 2D)$ that arise from minor dependencies on TI_∞.

In the fixed case, wake recovery increases with inflow turbulence. For example, $R_w(x = 10D)$ increases from approximately 0.7 at $TI_\infty = 1.1\ \%$ (dark blue in figure 9*a*) to about 0.83 at $TI_\infty = 5.8\ \%$ (light yellow in the same figure), in agreement with trends reported

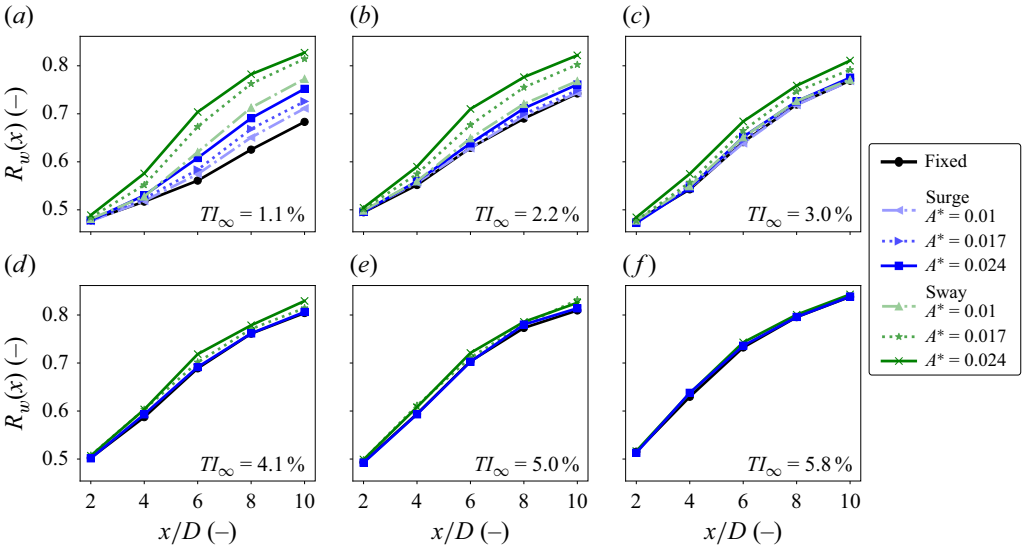

Figure 8. Wake recovery from (2.2) for different free-stream turbulence levels: $TI_\infty = 1.1\,\%{-}5.8\,\%$ (cases O1.1–O5.8 in table 1). Results include fixed ($St = 0$), surge and sway motions at $St = 0.3$ with $A^* \in \{0.01, 0.017, 0.024\}$ (table 2).

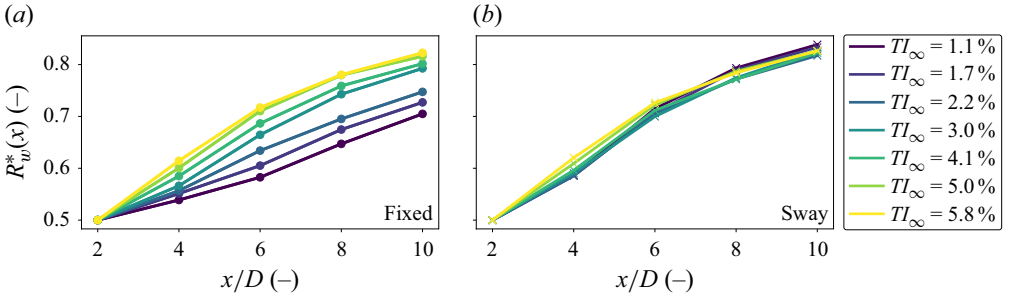

Figure 9. Offset-adjusted wake recovery: $R_w^*(x) = (R_w(x) - R_w(x = 2D)) + 0.5$ (R_w defined in (2.2) for different free-stream turbulence levels: $TI_\infty = 1.1\,\%{-}5.8\,\%$ (cases O1.1–O5.8 in table 1). Panel (*a*) shows the fixed case ($St = 0$) and panel (*b*) sway with $St = 0.3$ and $A^* = 0.024$ (table 2).

in the literature, such as Bastankhah & Porté-Agel (2014). This confirms the general observation that higher levels of free-stream turbulence lead to faster wake recovery.

In contrast, for the sway case with $A^* = 0.024$ (figure 9*b*), the recovery appears largely independent of inflow turbulence: $R_w(x = 10D) = 0.83 \pm 0.01$ across all TI_∞ levels. A slight effect of turbulence is visible around $x = 4D$, where higher turbulence modestly enhances recovery; however, this difference diminishes farther downstream. This suggests that while higher TI_∞ can slightly accelerate the onset of wake recovery, the influence of platform motion is substantially stronger. Remarkably, platform motion at low TI_∞ produces recovery levels equivalent to those achieved with high turbulence in the fixed case, emphasising the dominant role of platform movements in accelerating wake recovery. This effect is examined next in relation to motion-induced coherent structures.

3.3. *Motion-induced coherent structures with increasing TI_∞*

In figure 6 we found that coherent structures formed in the wake due to platform motion contribute to enhanced recovery by increasing the gradients of Reynolds shear

stresses in the $x-y$ and $x-z$ planes. However, as discussed in figures 8 and 9, this improvement diminishes with increasing TI_∞. To investigate the connection between this trend and the evolution of coherent structures at higher turbulence intensities, we examine the phase-resolved wake dynamics. The Oldenburg experiments, which use an array of 21 hot wires to simultaneously measure the streamwise velocity along a vertical line, enable the computation of $\widetilde{u}(\phi^*)$ at fixed streamwise positions. The measurements span $y \in [-1.4, 1.4]D$ and are synchronised – meaning that for a given x, all probes share the same initial phase ϕ_0.

We begin by analysing surge-induced periodic structures, illustrated in figure 10 for platform motion characterised by $St = 0.3$ and $A^* = 0.024$ (case surge-3-0.024 in table 2). Figure 10(a) shows contour plots of the combined mean and coherent streamwise velocity $(\overline{u} + \widetilde{u})/U_\infty$, while figure 10($b$) presents the coherent fluctuation component $\widetilde{u}/U_\infty$ alone. Each panel (a.-), (b.-) and (c.-) corresponds to a different inflow turbulence intensity, $TI_\infty \in \{1.1, 3.0, 5.8\}$ % – denoted as O1.1, O3.0 and O5.8 in table 1 – and spans one full oscillation cycle ($\phi^* \in [0, 2\pi]$) at downstream positions $x \in [2, 10]D$. At low turbulence ($TI_\infty = 1.1$ %), the combined velocity field shows a distinct periodic pattern of alternating bulges and constrictions, especially between $x \in [6, 8]D$ (see panels a.2–a.3 in figure 10a). The corresponding fluctuation fields in figure 10(b) (a.0)–(a.4) display in-phase red and blue bands – indicative of in-phase alternating speed-up and slow-down – characterising a pulsating wake. This structure is analogous to the varicose mode observed in a planar wake excited periodically in Wygnanski, Champagne & Marasli (1986). The pulsating structure is likely resulting from symmetric vortex roll-up in the shear layer due to the platform's surging motion. Similar patterns have been reported for thrust-excited and surging floating turbines in the studies of Yılmaz & Meyers (2018), Messmer *et al.* (2024*a*), Li & Yang (2024), Li *et al.* (2024), Wei *et al.* (2024), Hubert *et al.* (2025).

For $TI_\infty = 1.1$ %, coherent fluctuations reach amplitudes up to 15 % of the free-stream wind speed, underscoring the strong influence of platform motion under low turbulence conditions. The downstream evolution of the mode shows an initial low amplitude near $x = 2D$, which increases up to a peak around $x = 6D$ before decaying further downstream. This trend is consistent with observations at a fixed lateral position, which we reported in Messmer *et al.* (2024*a*). As TI_∞ increases, the amplitude of coherent fluctuations decreases substantially. At $TI_\infty = 3.0$ %, the pulsating pattern remains visible (see figure 10b (b.0)–(b.4)) but is less pronounced, with amplitudes reduced by a factor of approximately three. At the highest turbulence level ($TI_\infty = 5.8$ %), coherent structures are barely discernible, with amplitudes nearly six times lower than in the low turbulence case. At this level of inflow turbulence, the development of coherent wake structures is significantly inhibited, consistent with the CFD analysis of Yılmaz & Meyers (2018).

An equivalent analysis can be performed for sway motion. Figure 11 presents results for sideways platform motion characterised by $St = 0.3$ and $A^* = 0.024$ (case sway-3-0.024 in table 2), showing the same inflow conditions as for surge in figure 10. In contrast to surge, sway-induced platform motion causes strong lateral displacement of the wake, especially pronounced at $TI_\infty = 1.1$ % (see figure 11b (a.0)–(a.4)). The phase-averaged streamwise wake velocity, combined with the mean flow, exhibits a sinusoidal shape that causes the entire wake to oscillate laterally. This lateral motion contributes to the increased wake spreading observed in figure 7. For example, at $x = 8D$, the side-to-side amplitude of wake motion reaches approximately one rotor diameter, as shown by the y displacement between the wake centre at $\phi^* = 0$ and $\phi^* = \pi$ in figure 11(a) (a.3). This illustrates how the relatively small lateral rotor motion ($A_p = 0.024D$) is strongly amplified in the wake – a phenomenon we previously discussed in Messmer *et al.* (2024*a*) in terms of nonlinear dynamics.

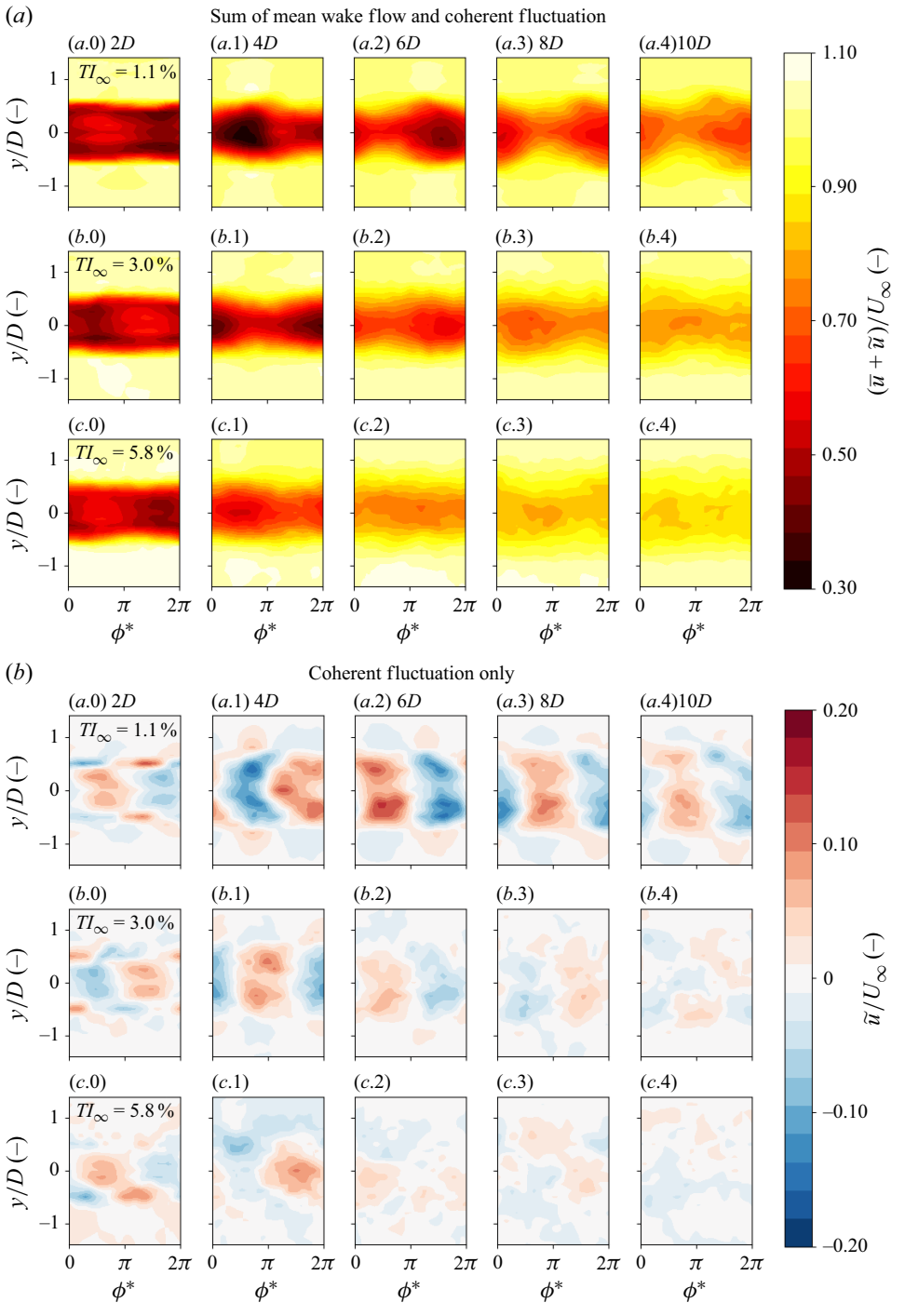

Figure 10. (*a*) Sum of the mean wake flow and the surge-induced coherent fluctuation. (*b*) Surge-induced coherent fluctuation alone. All velocities are normalised by the free-stream velocity U_∞. Columns (-.0)–(-.4) correspond to streamwise positions $x/D \in \{2, 4, 6, 8, 10\}$. Each panel represents one full period of the motion, shown over the normalised phase $\phi^* \in [0, 2\pi]$. Rows correspond to different inflow turbulence levels: (*a*.x) $TI_\infty = 1.1$ %, (*b*.x) $TI_\infty = 3.0$ % and (*c*.x) $TI_\infty = 5.8$ %, corresponding to cases O1.1, O3.0 and O5.8 in table 1. The motion parameters are $St = 0.3$ and $A^* = 0.024$ (case surge-3-0.024 in table 2).

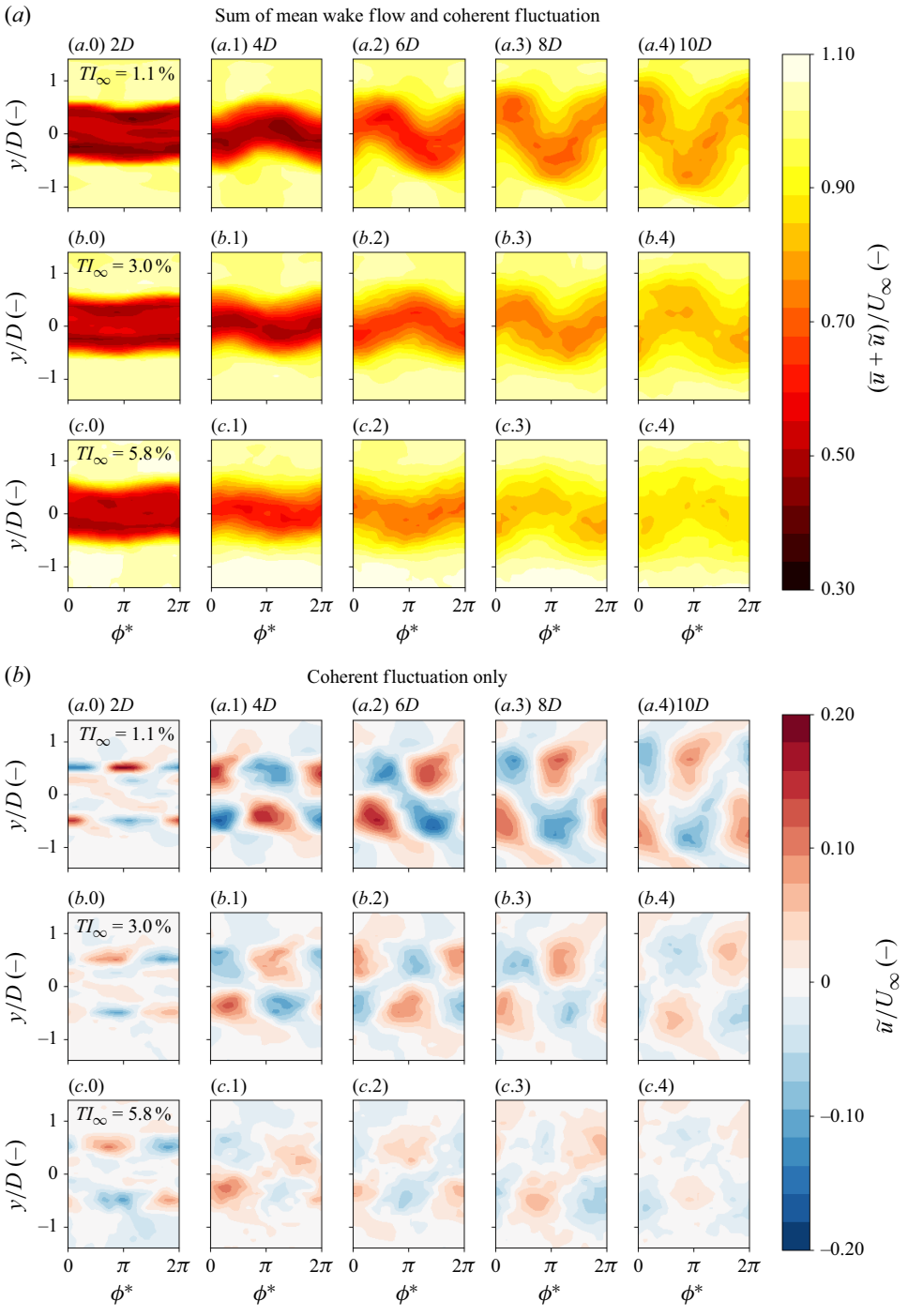

Figure 11. (*a*) Sum of the mean wake flow and the sway-induced coherent fluctuation. (*b*) Sway-induced coherent fluctuation alone. All velocities are normalised by the free-stream velocity U_∞. Columns (-.0)–(-.4) correspond to streamwise positions $x/D \in \{2, 4, 6, 8, 10\}$. Each panel represents one full period of the motion, shown over the normalised phase $\phi^* \in [0, 2\pi]$. Rows correspond to different inflow turbulence levels: (*a*.x) $TI_\infty = 1.1$ %, (*b*.x) $TI_\infty = 3.0$ % and (*c*.x) $TI_\infty = 5.8$ %, corresponding to cases O1.1, O3.0 and O5.8 in table 1. The motion parameters are $St = 0.3$ and $A^* = 0.024$ (case sway-3-0.024 in table 2).

Interestingly, the shape of the phase-averaged wake bears a resemblance to the flow past a cylinder undergoing vortex shedding, as described by Cantwell & Coles (1983), and also to the flow behind high-solidity porous disks (see the smoke visualisations in Cannon, Champagne & Glezer (1993)). The periodic lateral wake motion shares similarities with the sinuous mode identified by Wygnanski *et al.* (1986) in planar wakes and the coherent structures found in excited jets (Crow & Champagne 1971). These analogies suggest that many shear flows exhibit an intrinsic sinuous mode, which, when excited at the appropriate frequency or under favourable conditions (e.g. low turbulence and strong shear layers), can develop into large-scale coherent structures due to shear layer instabilities – even in the presence of background turbulence, as observed in our case. In the context of wind energy, this phenomenon is referred to as coherent wake meandering and studied in detail in Mao & Sørensen (2018), Li *et al.* (2022). In our case, the meandering motions are triggered by the lateral turbine movements.

Accordingly – and in contrast to the surge-induced structures – the meandering patterns in figure 11(*b*) (*a*.0)–(*a*.4) exhibit anti-phase velocity fluctuations: $\widetilde{u}(\phi^* = \pi,\ y = -R) \approx -\widetilde{u}(\phi^* = \pi,\ y = R)$. The amplitude of these streamwise meandering fluctuations reaches up to 20 % of the free-stream velocity. As with surge, increasing inflow turbulence reduces the magnitude of these coherent structures: at $TI_\infty = 3.0$ % amplitudes are roughly halved, while at $TI_\infty = 5.8$ % they are reduced by a factor of six. Similar to the results obtained for surge motion, the shape of the mode remains consistent across different turbulence intensities. Its magnitude increases with downstream distance, reaching a maximum between $x \in [4D,\ 6D]$, before gradually decaying further downstream.

Later in the paper, we quantify the energy contained in these coherent structures and examine the relationship between their energy content, wake recovery enhancement and the energy input from platform excitation. A direct comparison between surge and sway motions is presented to highlight the differences in their respective impacts.

Prior to this, we address and quantify a frequently debated issue in wind energy: the effect of coherent fluctuations on the time evolution of phase-resolved wake recovery.

3.4. *Coherent structures and phase-resolved wake recovery*

It is often argued that the observed increase in wake recovery – computed using (2.2) and shown in figure 8 – in response to platform motion or rotor excitation could be an artefact of periodic wake displacement, as discussed by Korb *et al.* (2023). This is particularly relevant in the case of sway-induced coherent structures (figure 11*a*), where the entire wake undergoes large-amplitude lateral oscillations. When such motion is averaged over time and across the rotor area, it can artificially smooth the wake profile, giving a feigned increased recovery. This raises an important question: Is the enhanced recovery a result of actual momentum exchange, or is it merely a consequence of averaging over periodic lateral displacements? In the following, we clarify this distinction and present evidence to evaluate the true contribution of coherent structures to enhance momentum exchange.

Figure 12(*a*) displays horizontal wind speed profiles in the wake at $x = 6D$. Panels 12(*a*)(*c–g*) show both the time-averaged wake profile and phase-resolved wake profiles for the surging turbine operating at $St = 0.3$, $A^* = 0.024$ and $TI_\infty = 1.1$ %. For comparison, the wake of the fixed (non-oscillating) turbine is also included. Similarly, the wake profiles for the swaying turbine under identical operating conditions are shown in figure 12(*a*)(*h–l*). We manually adjusted the phase origin ϕ_0 such that, for $\phi^* = 0$, the phase-resolved wake aligns most closely with the time-averaged profile.

As ϕ^* increases ($\phi^* \in [0,\ \pi]$), the surging turbine's wake initially contracts and exhibits higher wind speeds than the time-averaged case (see figure 12*a*(*c–e*)). To better illustrate

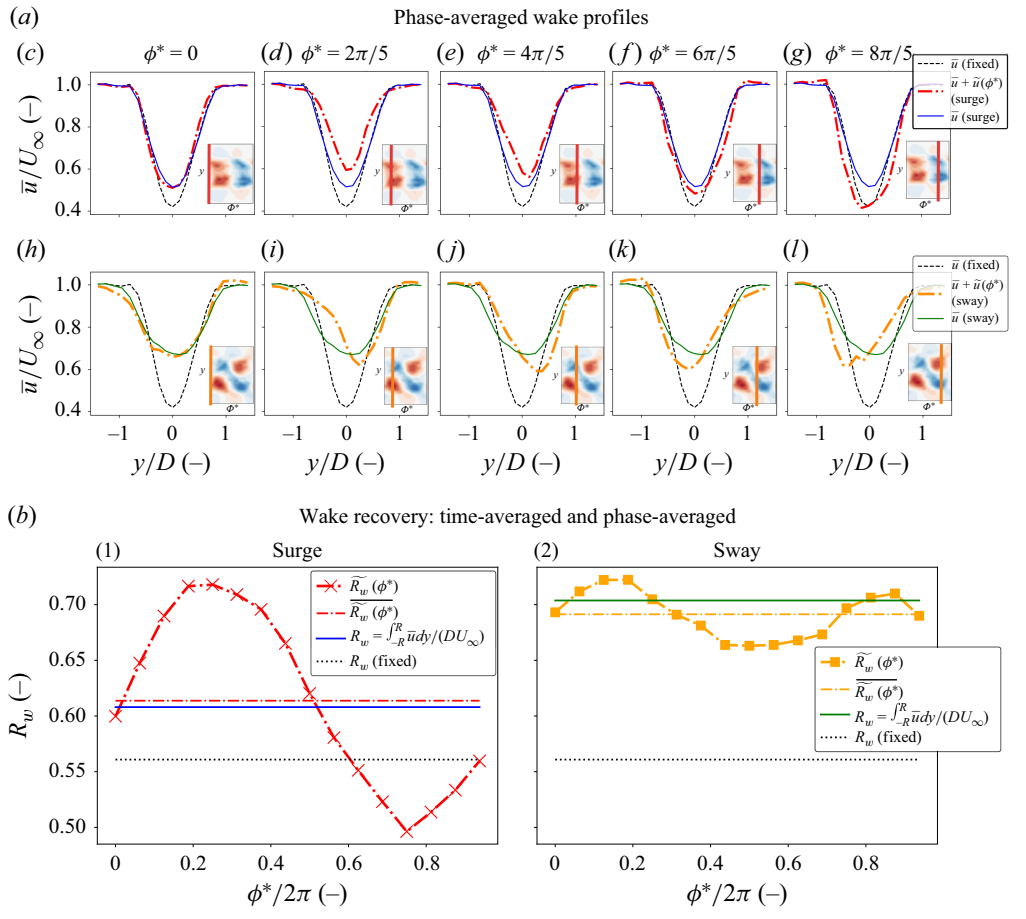

Figure 12. Comparison of time-averaged and phase-averaged wake recovery. (*a*) Time-averaged and local (phase-averaged) streamwise wind speed y profiles at $x = 6D$ for selected phases $\phi^* \in \{0, 2\pi, 4\pi, 6\pi, 8\pi\}/5$, for both surge (*a–e*) and sway (*f–j*) motions, with $St = 0.3$, $A^* = 0.024$ and $TI_\infty = 1.1\,\%$. (*b*) Local wake recovery $\widetilde{R_w}(\phi^*)$ computed across the phase range $\phi^*/2\pi \in [0, 1]$. The plot includes the mean of the phase-averaged recovery $\overline{\widetilde{R_w}(\phi^*)}$, the time-averaged recovery R_w (also for the fixed reference case), shown for both surge (1) and sway (2) cases.

the connection between the wake profiles and the coherent dynamics, we display in figure 12(*a*)(*c–e*) the structure previously shown in figure 10(*b*)(*a*.2), and mark with a red thick line the position of ϕ^*. Beyond $\phi^* > \pi$, the streamwise component of the coherent structure becomes negative, the wake expands, and the wind speed decreases below the time-averaged profile. Notably, at $\phi^* = 8\pi/5$, the wake speed is even lower than in the fixed case, i.e. $\overline{u}_{fixed} > (\overline{u} + \widetilde{u})_{surge}$.

To quantify the effects of motion on recovery at different phases, we define the phase-resolved wake recovery $\widetilde{R_w}(\phi^*)$ as

$$\widetilde{R_w}(\phi^*) = \frac{1}{DU_\infty} \int_{-R+y_c(\phi^*)}^{R+y_c(\phi^*)} \left(\overline{u} + \widetilde{u}(\phi^*)\right) \mathrm{d}y. \tag{3.2}$$

Here, $y_c(\phi^*)$ is the lateral location of the wake centre at a given phase, defined as the position where $\overline{u} + \widetilde{u}$ reaches its minimum. For surge motion, this position remains approximately constant and centred: $y_c(\phi^*) \approx 0$.

Figure 12(*b*)(1) shows the evolution of $\widetilde{R_w}$ over a full motion cycle ($\phi^*/2\pi \in [0, \sim 1]$), alongside the average, $\overline{\widetilde{R_w}}$, and the conventional time-averaged wake recovery from (2.2), both for the surging and fixed cases. In agreement with the profiles in figure 12(*a*)(*c–g*), the phase-resolved recovery initially increases (red x-. curves) when $\widetilde{u} > 0$ for $\phi^*/2\pi \in [0, 0.5]$. Then, as the wake expands for $\phi^*/2\pi > 0.5$, the recovery decreases, even falling below that of the fixed case. Overall, $\overline{\widetilde{R_w}}$ (red dashed line) is only slightly higher (by ~ 1 %) than the conventional time-averaged value (blue solid line). This indicates that, for surge motion, the coherent structures do not significantly alter the mean of the phase-averaged recoveries, although they do introduce large fluctuations depending on ϕ^*. As a result, downstream turbines in the wake would experience substantial power variability.

In contrast, the wake of the swaying turbine behaves differently. As seen in figure 12(*a*)(*h–l*), the wake undergoes significant lateral movement, with the wake centre $y_c(\phi^*)$ varying between $-R$ and R. This behaviour, driven by the meandering mode illustrated in figure 11(*b*)(*a*.2) and reproduced in figure 12(*a*)(*h–l*), causes the phase-averaged wake profile to shift side to side rather than contract or expand. Unlike the surge case, the minimum of $\overline{u} + \widetilde{u}$ remains almost constant across phases, but is slightly lower than that of the time-averaged wake alone. This suggests that the smoothed time-averaged profile (green solid line in figure 12(*a*)(*h–l*)) also includes a contribution from the phase displacements rather than solely from enhanced momentum transport.

Another important difference lies in the shape of the phase-resolved wake. For the surging turbine, the wake retains a near-Gaussian profile even locally, whereas the swaying turbine's wake becomes asymmetric at different phases – indicating a distortion caused by lateral motion. This further highlights the distinct nature of wake modulation between meandering and pulsating modes.

In figure 12(*b*)(2) we display the phase-averaged recovery for sway motion at various ϕ^* (orange squares), along with the average over all the phases, the time-averaged recovery and the fixed case for reference. Compared with the surge case, the variation in phase-resolved recovery is smaller ($\sim$6 % around the mean versus $\sim$16 % for surge). Interestingly, the time-averaged recovery (green solid line) is slightly greater than the mean of the phase-resolved wake recovery, however, by only about 3 %, indicating that the enhanced recovery for sway is primarily due to increased momentum transport rather than smoothing artefacts – a result also analysed by Korb *et al.* (2023). However, the approach of Korb *et al.* (2023) differs: using CFD, they examined energy differences between the time-averaged wake and the wake in a meandering frame of reference, integrated over the full wake area at a given downstream position. They reported differences up to 15 %, whereas our wind-speed-based line profiles show only a 3 % deviation. While the cases and metrics differ (they examined energy; we analyse streamwise velocity), both studies highlight that averaging over periodic wake motion introduces discrepancies in evaluating true recovery. If other metrics like $\overline{u^2}$ (kinetic energy) or $\overline{u^3}$ (wind power) were considered, these discrepancies would likely be more pronounced in our case. Nonetheless, we find that the dominant source of enhanced recovery remains the increased exchange between the wake and the outer flow – a point we return to in the conclusion.

3.5. *Coherent structures: energy perspectives*

We conclude the results section with an analysis of the energy of the coherent structures observed in the wake of the moving wind turbine, focusing on their relationship with free-stream turbulence intensity, energy of platform motion and enhanced wake recovery.

Reynolds & Hussain (1972) provide a mathematical framework for the energy dynamics of coherent structures, describing the transfer of energy between the mean flow, stochastic

fluctuations and coherent motions. They define the local kinetic energy of a coherent structure in a flow as

$$e_{CS} = \frac{1}{2}\overline{\widetilde{u}_i^{\,2}} = \frac{1}{2}\left(\overline{\widetilde{u}^2} + \overline{\widetilde{v}^2} + \overline{\widetilde{w}^2}\right). \tag{3.3}$$

In their work, Reynolds & Hussain (1972) derive a transport equation for e_{CS} from the phase-averaged Navier–Stokes equations. While such an analysis would be of interest in the present context, it falls beyond the scope of this study. However, the concept of energy remains relevant, as we can compute e_{CS} from the full 3-D dataset available from Milan, and evaluate $\overline{\widetilde{u}^2}$ (a subset of e_{CS}) across all cases with varying degrees of freedom (DoF), Strouhal number St, motion reduced-amplitude A^* and free-stream turbulence intensity TI_∞.

Hussain (1986) emphasises the 3-D nature of coherent structures, which often occupy a substantial volume of a sheared flow. This motivates extending the concept of local energy to a more spatially integrated quantity, particularly across the dimensions where measurements are available. Previous CFD studies from Yılmaz & Meyers (2018) and Li *et al.* (2022) provide visual evidence of the large-scale extent of these structures in 3-D space.

In our case, measurements are taken along a horizontal line at hub height. As observed in figures 10 and 11, the motion-induced coherent structures span a significant portion of the lateral direction. Most of the energy is concentrated in the region $y \in [-D, D]$, as illustrated, for example, in figure 11(*b*)(*a*.2). Based on this, and following a similar approach to Yılmaz & Meyers (2018), we define the spanwise-integrated kinetic energy of the coherent structures, normalised by the inflow mean kinetic energy:

$$E^*_{CS} = \frac{1}{2D}\int_{-D}^{D} \frac{1}{2}\left(\overline{\widetilde{u}^2} + \overline{\widetilde{v}^2} + \overline{\widetilde{w}^2}\right)\mathrm{d}y \Big/ \left(\frac{1}{2}U_\infty^2\right) = \frac{1}{2DU_\infty^2}\int_{-D}^{D} e_{CS}\,\mathrm{d}y. \tag{3.4}$$

To enable comparison across all datasets, we also define a streamwise-only version, $E^*_{x,CS}$, which uses only the streamwise component $\overline{\widetilde{u}^2}$:

$$E^*_{x,CS} = \frac{1}{2DU_\infty^2}\int_{-D}^{D} \overline{\widetilde{u}^2}\,\mathrm{d}y. \tag{3.5}$$

Similar to (3.5), we define $E^*_{y,CS}$ and $E^*_{z,CS}$ as the normalised energy contributions from the spanwise ($\overline{\widetilde{v}^2}$) and vertical ($\overline{\widetilde{w}^2}$) components of the coherent structures, respectively.

We begin by examining the shared dataset between Milan and Oldenburg for the cases surge-5 and sway-5 (see table 2), under inflow conditions M1.5 and O1.5 with $TI_\infty = 1.5\,\%$ (see table 1). Figure 13(*a*) presents the downstream evolution of $E^*_{x,CS}$ from both the Milan and Oldenburg datasets, while figure 13(*b*) shows the evolution of $E^*_{i,CS}$, where $i \in \{x, y, z\}$, and the total energy E^*_{CS}, using the 3-D data from Milan. The good agreement (i.e. a mean deviation of less than 10 %) between the curves marked with empty symbols (Oldenburg) in figure 13(*a*) and those with filled symbols (Milan) confirms the consistency of the results from the two experiments. A more detailed comparison is provided in Appendix B.

In figure 13(*a*) the normalised, spanwise-integrated energy of $\overline{\widetilde{u}^2}$ for both surge- and sway-induced structures initially increases for $x \lesssim 4D$. This indicates that, in the near-wake to the transition region, the coherent structures are gaining energy. The energy associated with the meandering mode (sway, green curve) is approximately 50 % larger than that of the pulsating mode (surge), correlating with the higher wake recovery for sway observed in figure 4(*a*). Further downstream, for $3.5 \lesssim x/D \lesssim 5.5$, the energy reaches a

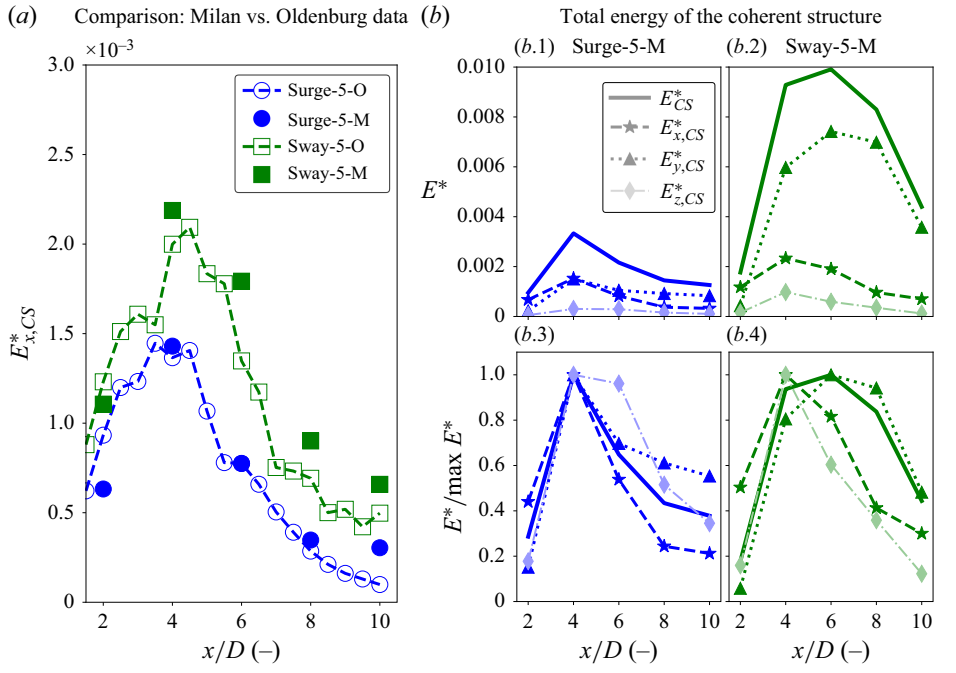

Figure 13. Integrated energy of surge- and sway-induced coherent structures for cases surge-5 and sway-5 (see table 2). (*a*) Comparison of the integrated energy of the streamwise component of the coherent fluctuations $E^*_{x,CS}$ (3.5) for surge and sway with $St = 0.38$, $A^* = 0.01$, using Milan and Oldenburg datasets ($TI_\infty = 1.5$ %). (*b*) Integrated energy of each component of the coherent structure: streamwise $\widetilde{u^2}$, lateral $\widetilde{v^2}$ and vertical $\widetilde{w^2}$ velocities, as well as their total noted $E^*_{x,CS}$, $E^*_{y,CS}$, $E^*_{z,CS}$ and E^*_{CS}, respectively, for surge (*b*.1) and sway (*b*.2). Panels (*b*.3) and (*b*.4) show the same energy components normalised by their respective maximum values.

peak and then decays. This decline indicates that the coherent structures are dissipating energy, consistent with our pointwise analysis in Messmer *et al.* (2024*a*). By $x = 10D$, the energy has dropped to about one-fifth of its peak value, showing strong dissipation and potential breakdown into smaller-scale turbulence, consistent with the classic energy cascade described by Richardson/Kolmogorov (Pope 2001).

Figure 13(*b*)(1–2) provide additional insights into the downstream development of $E^*_{y,CS}$, $E^*_{z,CS}$ and the total E^*_{CS} for the Milan dataset. The differences between the surge- and sway-induced structures are much more pronounced when considering the full 3-D energy components. In particular, the spanwise component $\widetilde{v^2}$ (triangular markers with dashed lines) shows almost four times more energy for sway than for surge. As a result, the total energy E^*_{CS} is nearly three times higher for sway, emphasising the energetic dominance of the meandering mode under identical excitation conditions ($St = 0.38$, $A^* = 0.01$).

Despite these differences, the overall trends are similar: E^*_{CS} increases to a peak before decreasing downstream. This full 3-D analysis shows that a significant portion of the meandering mode's energy resides in the spanwise direction ($\widetilde{v}$), as expected from its lateral motion characteristics. Figure 13(*b*).(3–4) show the same quantities as in *b*.(1–2), but normalised by their respective maximum values. While the normalised total energy $E^*_{CS}/\max E^*_{CS}$ does not exactly match the normalised streamwise component $E^*_{x,CS}/\max E^*_{x,CS}$, the trends remain consistent. This supports the decision to investigate $E^*_{x,CS}$ as a proxy for total energy across all cases – while acknowledging that it only

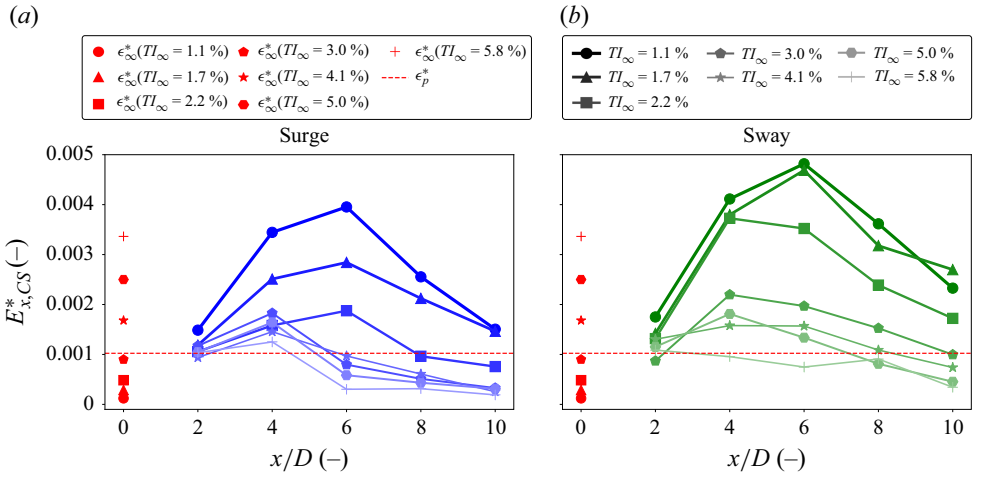

Figure 14. Integrated energy of the streamwise component of the coherent structures induced by motions $E^*_{x,CS}$ for surge (*a*) and sway (*b*) both with $St = 0.3$, $A^* = 0.024$ (surge- and sway-3–0.024 in table 2) for $TI_\infty \in [1.1, 5.8]$ % (O1.1–O5.8 in table 1). The red symbols represent the normalised energy of the free-stream fluctuations ϵ^*_∞ (3.6) and the dashed line shows ϵ^*_p, the normalised energy of the platform motion (3.7).

represents a portion of the total energy. In particular, for the meandering mode (sway), a large fraction of the total energy is concentrated in the spanwise component $E^*_{y,CS}$, meaning that differences between surge and sway are more significant than suggested by $E^*_{x,CS}$ alone. Nonetheless, it is reasonable to assume that a lower $E^*_{x,CS}$ generally implies a lower total energy E^*_{CS}.

We next analyse the $E^*_{x,CS}$ dependency to inflow conditions and motion parameters. We start with figure 14 for the normalised energy evolution of the pulsating mode from surge motion (figure 14*a*) and meandering mode from sway (figure 14*b*) both with $St = 0.3$, $A^* = 0.024$ for the different inflows: $TI_\infty \in [1.1, 5.8]$ %. On both panels, we added red symbols that represent the normalised energy of the free-stream fluctuations, ϵ^*_∞, defined as

$$\epsilon^*_\infty = \epsilon_\infty / \left(1/2U^2_\infty\right) = \left(1/2\overline{u'^2_\infty}\right) / \left(1/2U^2_\infty\right) = \overline{u'^2_\infty} / U^2_\infty = TI^2_\infty. \tag{3.6}$$

From (3.6), the higher the inflow TI_∞, the higher the energy of the fluctuations. Here ϵ^*_∞ can be compared with $E^*_{x,CS}$ as well as the normalised energy of the platform motion, ϵ^*_p, which we defined and discussed already in Messmer *et al.* (2024*a*), as

$$\epsilon^*_p = 2(\pi St A^*)^2, \tag{3.7}$$

which quantifies the normalised energy of the platform motion. Figure 14 illustrates that, for both surge (figure 14*a*) and sway (figure 14*b*), increasing inflow turbulence intensity TI_∞ (i.e. higher ϵ^*_∞) leads to a reduction in the energy of the coherent structures. This trend is also visible in figures 10 and 11, based on the spatial maps of $\widetilde{u}$.

For example, in the surge case, the normalised streamwise energy of the coherent structure, $E^*_{x,CS}$, is approximately eight times larger for $TI_\infty = 1.1$ % than for $TI_\infty = 5.8$ %. A similar trend is observed for sway, with the energy about five times higher at low turbulence. At a fixed inflow condition, sway-induced coherent structures exhibit higher energy levels than those induced by surge, consistent with the observations in figure 13(*a*).

Both surge and sway exhibit a similar evolution in coherent structure energy: an initial growth up to $x \approx 4{-}6D$, followed by a downstream decay. At $x = 2D$, the energy

levels are nearly identical across all inflow turbulence intensities TI_∞, and closely match ϵ_p^* – the energy associated with platform motion. This suggests that at this early position, the coherent structures have not yet developed and their energy is primarily determined by the imposed motion. Further downstream, however, the growth and peak level of coherent structure energy become strongly dependent on TI_∞. For low turbulence intensities ($TI_\infty \leqslant 2.2\,\%$), the structures grow substantially in energy. In contrast, for higher turbulence levels ($TI_\infty > 3\,\%$), their growth is significantly dampened. The location of the peak energy $E^*_{x,CS}$, as well as the rate of energy increase and decay, vary depending on both the direction of motion and TI_∞. This indicates that the formation and evolution of coherent structures are highly sensitive to inflow conditions.

Under surge excitation, when the inflow turbulence intensity exceeds approximately $TI_\infty \gtrsim 3\,\%$, the energy of the streamwise coherent structure, $E^*_{x,CS}$, generally falls below the platform motion energy threshold ϵ_p^*. While a slight increase above ϵ_p^* is observed close to the source, it quickly diminishes downstream, suggesting that higher turbulence intensity inhibits the formation and persistence of coherent structures. For sway, by contrast, coherent structure energy remains above the threshold until turbulence levels exceed approximately 5 %, demonstrating that the sway-induced structures are more resilient to free-stream turbulence.

Interestingly, this energy threshold seems to correlate with the wake recovery trends shown in figure 8. In the surge case, no significant improvement in recovery is observed for $TI_\infty \gtrsim 3\,\%$, whereas for the sway case, this limit rises to $TI_\infty \gtrsim 5\,\%$. This suggests that ϵ_p^* may act as a critical threshold – below which the coherent structure's energy is too weak to affect wake recovery meaningfully. Figure 14 also highlights that sway-induced structures not only carry more energy but also better resist the damping effects of increased inflow turbulence compared with surge-induced structures.

So far, we have investigated only the highest amplitude of motion ($A^* = 0.024$). We now extend the analysis in figure 15 to include all three tested amplitudes: $A^* \in \{0.01,\ 0.017,\ 0.024\}$. To facilitate the analysis of how coherent structure energy depends on A^* and inflow turbulence intensity TI_∞, we introduce a streamwise-integrated metric.

As shown in figure 14, increasing levels of TI_∞ lead to a clear reduction in the overall energy of the coherent structures. On average, this energy is well above the platform motion energy threshold ϵ_p^* for low turbulence levels ($TI_\infty < 2\,\%$), approximately equal to it around $TI_\infty \approx 3\,\%$, and falls below it for higher turbulence intensities ($TI_\infty > 3\,\%$) in the surge case (figure 14*a*). For sway, the thresholds are at higher TI_∞ values (figure 14*b*). These observations motivate the use of a spatially integrated metric that captures the overall strength of the structure and allows direct comparison with ϵ_p^*. Inspired by the approach of Yılmaz & Meyers (2018), we define the streamwise-integrated coherent structure energy as

$$\int E^*_{x,CS} = \frac{1}{8D}\int_{x=2D}^{x=10D} E^*_{x,CS}(x)\,\mathrm{d}x. \tag{3.8}$$

This quantity represents a spatially averaged estimate of the coherent structure energy in the x direction, computed over the region where the structures are observed ($x \times y \in [2D,\ 10D] \times [-D,\ D]$). Figure 15 presents $\int E^*_{x,CS}$ as a function of inflow turbulence intensity TI_∞ for surge (*a*) and sway (*b*) excitation, at fixed Strouhal number $St = 0.3$, and for all amplitudes and inflow conditions considered (O1.1–O5.8 in table 1, corresponding to $TI_\infty \in [1.1\,\%,\ 5.8\,\%]$).

A consistent trend is observed for both motion directions: for a given inflow condition, increasing A^* leads to a higher coherent structure energy. For example, at $TI_\infty = 1.1\,\%$, the integrated energy for surge at $A^* = 0.024$ is approximately three times higher than at

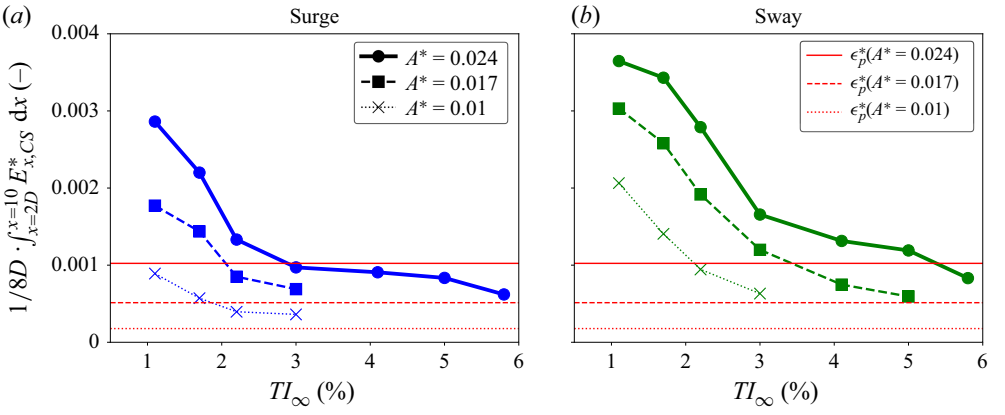

Figure 15. Streamwise-integrated energy of the coherent structures in the x direction, defined as $\int E_{x,CS}^* = (1/8D) \int_{x=2D}^{x=10D} E_{x,CS}^*(x) \, \mathrm{d}x$, plotted against the inflow turbulence intensity TI_∞ for (*a*) surge and (*b*) sway. All cases use $St = 0.3$ and $A^* \in \{0.01,\ 0.017,\ 0.024\}$ in table 2 and inflows O1.1–O5.8 in table 1. Here red :, –,- lines represent ϵ_p^* defined in (3.7).

$A^* = 0.01$ (compare blue • and x in figure 15*a*). Similarly, for sway, the increase is about 1.8 times (compare green • and x in figure 15*b*).

A higher A^* naturally results in a higher excitation energy ϵ_p^*, which scales with A^{*2} (3.7). Thus, the platform motion at $A^* = 0.024$ carries approximately 5.8 times more energy than at $A^* = 0.01$. Interestingly, the relative response of the wake structures (i.e. the energy of the structures relative to ϵ_p^*) is larger for smaller A^*, which aligns with classical findings in periodic excitation and synchronisation theory. As shown by Pikovsky *et al.* (2001), weakly forced nonlinear systems often exhibit enhanced sensitivity, leading to more efficient energy amplification at lower excitation amplitudes. Nonetheless, in terms of absolute energy levels, our results show clearly that increasing the excitation amplitude leads to more energetic coherent structures. Since $\epsilon_p^* \ll 1$, even the largest tested amplitudes still fall in the range of what can be considered infinitesimal forcing.

The further analysis of figure 15 confirms, as previously analysed in figure 14, that sway motion generates coherent structures with higher energy and greater resilience to increasing inflow turbulence intensity TI_∞, compared with surge. The connection between the energy of the coherent structures and wake recovery enhancement becomes apparent: as TI_∞ increases, the energy of the structures decreases, and so does the impact of the structures on recovery. For the largest amplitude $A^* = 0.024$, the energy drops below the corresponding platform motion energy $\epsilon_p^*(A^* = 0.024)$ at approximately $TI_\infty \approx 3.0\,\%$ for surge and $TI_\infty \approx 5.0\,\%$ for sway. For the lower amplitudes ($A^* \leqslant 0.017$), $\int E_{x,CS}^*$ remains above the respective $\epsilon_p^*(A^*)$ for all inflow conditions, but the absolute energy remains significantly lower than that of the structures induced by $A^* = 0.024$. By linking figures 8 and 15, we observe that, for any A^*, when $\int E_{x,CS}^* \lesssim \epsilon_p^*(A^* = 0.024)$, the impact of platform motion on wake recovery improvement becomes negligible. Therefore, the higher energy of the meandering structures induced by sway, along with their greater robustness to increasing TI_∞, leads to an extended range of inflow turbulence conditions where sway motion improves recovery compared with surge. This observation is further quantified in figure 16.

Figures 14 and 15 have shown that both ϵ_∞^* (the normalised energy of the free-stream fluctuations) and ϵ_p^* (the normalised energy of the platform motion) are key

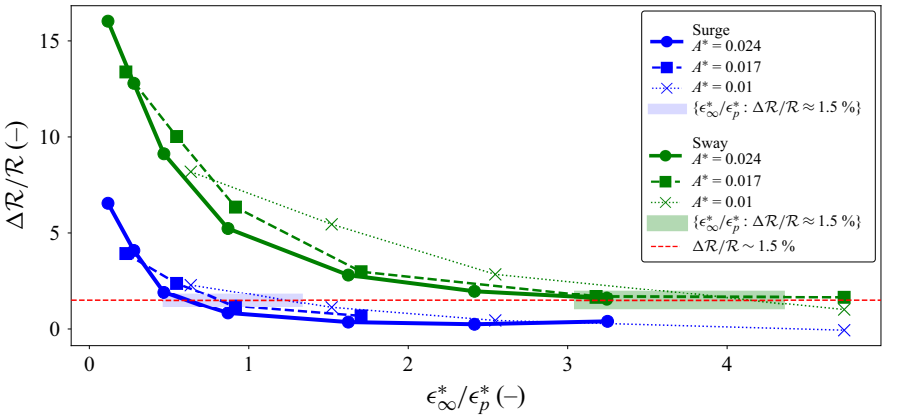

Figure 16. Relative increase in wake recovery, $\Delta\mathcal{R}/\mathcal{R}$ (3.10), plotted against the ratio $\epsilon^*_\infty/\epsilon^*_p$, which compares the normalised energy of free-stream fluctuations to that of platform motion. Data includes all motion cases with $St = 0.3$ and inflow conditions from O1.1 to O5.8 (see tables 1 and 2). A threshold of 1.5 % is shown as a red dashed line.

parameters governing the energy of coherent structures and, consequently, the wake recovery enhancement. An increase in ϵ^*_p leads to more energetic structures for a fixed ϵ^*_∞, while an increase in ϵ^*_∞ results in weaker structures, as they struggle to emerge and persist in a more turbulent background at constant ϵ^*_p. As the energy of the coherent structures decreases, so does their impact on wake recovery improvement.

This observation motivates the study of the relative increase in wake recovery, $\Delta\mathcal{R}/\mathcal{R}$, between a case with platform motion and the corresponding fixed-platform reference, for different energy levels of inflow and platform motion. The streamwise-integrated wake recovery $\mathcal{R}$ is defined as

$$\mathcal{R} = \frac{1}{8D}\int_{x=2D}^{x=10D}\frac{1}{D}\int_{y=-R}^{y=R}\frac{\overline{u}(x,\,y)}{U_\infty}\,\mathrm{d}y\,\mathrm{d}x = \frac{1}{8D}\int_{x=2D}^{x=10D} R_w(x)\,\mathrm{d}x. \tag{3.9}$$

Here, $\mathcal{R}$ represents the average recovery over the measurement region $x \in [2D,\,10D]$. The relative increase in recovery is given by

$$\frac{\Delta\mathcal{R}}{\mathcal{R}} = \frac{\mathcal{R}(St,\,A^*,\,\mathrm{Dof},\,TI_\infty) - \mathcal{R}(St=0,\,TI_\infty)}{\mathcal{R}(St,\,A^*,\,\mathrm{Dof},\,TI_\infty)}. \tag{3.10}$$

This quantity quantifies the relative improvement in wake recovery due to platform motion, averaged over the streamwise measurement domain. The final figure 16 shows the evolution of $\Delta\mathcal{R}/\mathcal{R}$ (3.10), plotted against the ratio $\epsilon^*_\infty/\epsilon^*_p$ for all motion cases with $St = 0.3$ and inflows ranging from O1.1 to O5.8. This figure complies some of the outcomes of figures 8, 14 and 15 combined.

For $TI_\infty = 1.1$ %, $\epsilon^*_\infty = 1.2 \times 10^{-4}$, which is lower than ϵ^*_p for all A^*. For example, for $A^* = 0.024$, $\epsilon^*_\infty/\epsilon^*_p \approx 0.1$, indicating that there is an order of magnitude more energy in the platform motion than in the free-stream turbulence. As a result, the energy of the coherent structure found in the wake and induced by the platform is significant (the largest) for both surge and sway DoFs (see the blue and green • in figure 15(a) and 15(b) for quantification). Consequently, the impact on recovery is also large: about 16 % more averaged recovery is observed for sway compared with 7 % for surge, relative to the fixed case's recovery (see the • points for $\epsilon^*_\infty/\epsilon^*_p \approx 0.1$ in figure 16). As $\epsilon^*_\infty/\epsilon^*_p$ increases, the inflow turbulence either increases (if ϵ^*_p is fixed) or ϵ^*_p decreases (with

fixed ϵ^*_∞). Regardless of the scenario, as $\epsilon^*_\infty/\epsilon^*_p$ increases, the relative importance of the motion diminishes because the inflow turbulence becomes more dominant. For both surge and sway, small discrepancies in the impact of motion on recovery improvement can be observed at different amplitudes for a given $\epsilon^*_\infty/\epsilon^*_p$ ratio. Specifically, the lowest amplitude (x in figure 16) leads to larger recovery improvements compared with the highest amplitude, consistent with the statement that 'the lower the excitation amplitude, the greater the relative impact'. Nevertheless, the overall trend remains clear: as $\epsilon^*_\infty/\epsilon^*_p$ increases, the influence of platform motion on wake recovery diminishes, eventually falling below 1.5 % – a level at which the effect becomes indistinguishable from measurement uncertainty here (Messmer *et al.* 2024*b*).

Notably, the difference between surge and sway, discussed throughout the paper, becomes evident here. For $\epsilon^*_\infty/\epsilon^*_p \gtrsim 1$ (marked with the transparent blue rectangle in figure 16), the impact of surge motion on wake recovery becomes negligible. In contrast, the threshold for sway is about 3.5 times higher, with no measurable impact for $\epsilon^*_\infty/\epsilon^*_p \gtrsim 3.5$. This key result demonstrates that surge-induced coherent structures, responsible for enhanced recovery, are more sensitive to inflow turbulence than sway-induced structures, with a factor of about 3.5. This is further discussed in the conclusion.

4. Summary of the main findings

In this paper we investigated wake recovery mechanisms and the interplay between inflow turbulence and motion-induced coherent structures in the wake of a model floating wind turbine. We considered harmonic surge and sway motions (figure 2*b*,*c*), with motion parameters $St \in \{0.3, 0.38\}$ and $A^* \in \{0.01, 0.017, 0.024\}$. Wind tunnel experiments (figure 1) were conducted in two facilities under various inflow conditions, with turbulence intensities $TI_\infty \in [1.1, 5.8]$ %, controlled using an active grid. Hereafter, we summarise the main findings.

The new insights of this paper are the connection between motion-induced coherent structures and enhanced wake recovery, as well as the interplay with increasing TI_∞.

First, at $TI_\infty = 1.5$ %, we found that the increased wake recovery with platform motion, most pronounced for sway (figure 4*a*), is directly linked to an increase (up to 65 % more than the fixed reference case) in the Reynolds shear stress gradient term in the x–y plane (i.e. from streamwise-lateral fluctuations), and secondly in the x–z plane. Previous work by Bastankhah & Porté-Agel (2016), Boudreau & Dumas (2017), van der Laan *et al.* (2023), Gambuzza & Ganapathisubramani (2023) identified these terms as the main drivers of recovery. In this paper we further decompose the terms $-\langle(1/\overline{u})(\partial\overline{u'v'}/\partial y + \partial\overline{u'w'}/\partial z)\rangle$ as the sum of the contributions from the coherent structure ($\widetilde{\widetilde{u}}\widetilde{\widetilde{v}}$, $\widetilde{\widetilde{u}}\widetilde{\widetilde{w}}$) and purely stochastic turbulence ($\overline{u''v''}$, $\overline{u''w''}$). We showed in figure 6 the large contribution (more than 50 %) from $-\left\langle(1/\overline{u})\partial\widetilde{\widetilde{u}}\widetilde{\widetilde{v}}/\partial y\right\rangle$, i.e. from the coherent structure induced by the rotor motion of the floating platform to the improved $-\langle(1/\overline{u})\partial\overline{u'v'}/\partial y\rangle$. This term is found in the wake recovery rate budget (2.6) and contributes to the higher recovery rate, $D\partial R_w/\partial x$. This new result confirms our speculation in Messmer *et al.* (2024*a*) and provides clear evidence as well as quantification of the role of large-scale coherent structures in improving wake recovery.

Second, as TI_∞ increases, the wake recovery of the moving turbine approaches that of the fixed case, indicating that higher inflow turbulence reduces the influence of motion on recovery enhancement (figure 8). This trend is consistent with CFD results for sway motion reported by Li *et al.* (2022) and surge motion from Li *et al.* (2024), as well as with other rotor excitation techniques investigated in Yılmaz & Meyers (2018), Korb *et al.* (2023).

We considered three amplitudes of motion and observed that higher amplitudes result in a more pronounced impact on recovery. Comparing fore-aft and sideways motion, we saw in figure 8 that sway motion leads to a larger increase in recovery than surge for equivalent cases. Furthermore, this study identifies the inflow turbulence levels, TI_∞, beyond which the impact of platform motion on wake recovery becomes negligible. Specifically, for the maximum amplitude tested ($A^* = 0.024$ at $St = 0.3$), the critical threshold is approximately $TI_\infty \approx 3\,\%$ for surge and $TI_\infty \approx 5\,\%$ for sway motion.

Third, the measurements from Oldenburg enabled the computation of the shape of the coherent structures and allowed us to distinguish two different modes induced by surge (fore-aft) and sway (sideways) motion, as well as their development under increasing free-stream turbulence. Fore-aft motion leads to the formation of pulsating coherent structures (figure 10), characterised by alternating shrinking and expansion of the wake, also reported in Yılmaz & Meyers (2018), Li & Yang (2024), Li *et al.* (2024), Wei *et al.* (2024), Hubert *et al.* (2025), and resembling the varicose mode observed in planar wakes described by Wygnanski *et al.* (1986). In contrast, sway motion generates structures that oscillate side to side, a typical meandering mode, similar to those found and discussed in Li *et al.* (2022), Li & Yang (2024). This structure shares characteristics with vortex shedding behind bluff bodies (see figure 11) and with the sinous mode described by Wygnanski *et al.* (1986). Both types of structures (pulsating and meandering) contribute to increased Reynolds shear stresses, $\partial\overline{u'v'}/\partial y$ and $\partial\overline{u'w'}/\partial z$, as discussed earlier and shown in figure 6. For both DoF, increasing the level of inflow turbulence, TI_∞, leads to less pronounced coherent structures, which become barely visible at $TI_\infty = 5.8\,\%$.

Fourth, we investigated the influence of coherent structures on phase-resolved wake recovery, by examining changes in the phase-resolved wake profiles (figure 12). Surge motion induces significant phase-to-phase variations in wake recovery, but these fluctuations average out over a cycle to result in little to no difference in the average of the phase-averaged recoveries compared with the time-averaged recovery defined in (2.2). Sway motion, in contrast, causes smaller phase-to-phase fluctuations, yet the mean phase-resolved recovery is lower than the classic time-averaged recovery. This suggests, as also noted by Korb *et al.* (2023), that part of the enhanced wake recovery observed with sway motion, reflected in the increased term $\partial\overline{u'v'}/\partial y$, is due to lateral smearing of the wake profile. However, this smearing mechanism accounts for only about 10 % of the total recovery enhancement, indicating in our case that the dominant contribution arises from increased momentum entrainment.

Finally, we linked enhanced recovery and coherent structures by examining the energy of the large-scale organised patterns. We focused on the streamwise component of the coherent structure energy, $E^*_{x,CS}$ (3.5), and provided rationale for this choice in figure 13. Results show that meandering structures exhibit higher energy and are more resilient to increasing inflow turbulence than surge-induced structures (figure 14). Moreover, higher motion amplitudes, A^*, generate structures with greater energy compared with lower amplitudes, directly linking to the lower recovery increase under smaller motion amplitudes (figure 15). Last but not least, we quantified the relationship between the energy of free-stream fluctuations, ϵ^*_∞ (3.6), and that of the platform motion, ϵ^*_p (3.7), in relation to the relative increase in wake recovery (figure 16). For $\epsilon^*_\infty/\epsilon^*_p < 0.5$, i.e. when motion energy dominates over free-stream fluctuations, both surge and sway motions enhance wake recovery, with sway leading to up to 16 % improvement. However, as ϵ^*_∞ increases, the impact of motion on recovery diminishes. Our results clearly show that sway consistently leads to larger recovery enhancement than surge and that sway-induced structures are more resilient to inflow turbulence. We found that, for $\epsilon^*_\infty/\epsilon^*_p \gtrsim 1$, the

effect of surge motion on wake recovery improvement becomes negligible, while for sway, this threshold is about $\epsilon^*_\infty/\epsilon^*_p \gtrsim 3.5$, indicating the greater robustness of sway-induced structures to free-stream turbulence.

5. Discussion and conclusion

Last, we discuss and draw conclusions based on our results regarding the similarity with canonical flows and local wake recovery mechanisms (§ 5.1), the formation of coherent structures in turbulent backgrounds (§ 5.2) and the implications for wind energy (§ 5.3).

5.1. *Similarities with canonical flows and local wake recovery mechanisms*

Despite the complexity of wind turbine wakes and the high Reynolds numbers involved, it is remarkable to observe wake dynamics similar of those found in canonical shear flows with laminar backgrounds, as described in foundational studies from the 1970s and 1980s (Crow & Champagne 1971; Ho & Huerre 1984; Wygnanski *et al.* 1986). These structures arise from shear-flow instabilities, where periodic disturbances are strongly amplified (Gupta & Wan 2019), even in turbulent environments where excitations are less distinct. In the wake of a fixed turbine, we observed inherent sinuous (Wygnanski *et al.* 1986) (i.e. meandering) modes, as evidenced by the erratic meandering reported in Messmer *et al.* (2024*a*). However, these modes are typically smeared out, resulting in disorganised motion similar to that observed behind porous disks with high porosity (Cannon *et al.* 1993). This behaviour occurs within a characteristic meandering frequency range (f_m), defined by the Strouhal number $St_m = (f_m D/U_\infty) \in [0.1, 0.5]$, as previously discussed in Messmer *et al.* (2024*a*). When such a shear flow is excited at an appropriate frequency (e.g. $f_p D/U_\infty \approx 0.3$), via harmonic platform motion or other methods, the convectively unstable wake responds strongly, even to small perturbations (Ho & Huerre 1984). The dynamics then become dominated by the excited coherent structures, similar to vortex shedding behind a cylinder. As noted by Cantwell & Coles (1983), 'the relatively large stress associated with deep incursions of free-stream fluid into the regions between the (coherent) vortices' is the 'most interesting feature' of such flows. This observation raises questions about the local mechanisms driving wake recovery, which we discuss in the following.

Our findings demonstrate that, in a time-averaged sense, large-scale periodic structures enhance wake recovery by increasing the gradient of the Reynolds shear stresses. Instantaneously, two key mechanisms appear to be involved: periodic wake deflection (Korb *et al.* 2023) and enhanced entrainment – achieved via engulfment and nibbling processes, as discussed by Kankanwadi & Buxton (2020) in the context of cylinder wakes. As shown in figure 12, the majority of the recovery enhancement originates from increased entrainment, while wake deflection plays a secondary role.

An open question remains: Which local entrainment mechanism is primarily enhanced by the presence of large-scale structures – nibbling, engulfment, or both? On one hand, the organised structures likely increase the length of the interface between the wake and the outer flow (i.e. the turbulent–turbulent interface), potentially enabling enhanced momentum transfer via small-scale nibbling (da Silva *et al.* 2014). On the other hand, following the observations of Cantwell & Coles (1983), large-scale structures may promote engulfment by drawing outer fluid into the wake core, thereby accelerating momentum recovery.

At this stage, these remain hypotheses, but they represent promising directions for future investigation aimed at better understanding the very local mechanisms by which large-scale coherence influences wake recovery.

5.2. *Formation of excited coherent structures in a turbulent background*

In this paper we turned to analytical methods originally used to study coherent structures in canonical flows (Reynolds & Hussain 1972), applying them here to measure structures' energy and its dependence on free-stream turbulence to a problem motivated by wind energy. We observed that increased inflow turbulence (TI_∞) leads to less energetic motion-excited coherent structures. This suggests that higher turbulence levels either smear out the periodic excitation, preventing the formation of coherent structures, or disrupt the structures rapidly, or both. We found that reduced coherent structure energy corresponds to weaker enhancements in the Reynolds stress gradients, as evidenced by the comparison between surge- and sway-induced structures in figure 13(*b*.1,*b*.2). The reduced surge-induced structure energy is further linked to the diminished $\partial\overline{u'v'}/\partial y$, $\partial\overline{u'w'}/\partial z$ observed in figure 6(*e*) compared with figure 6(*f*) for sway, highlighting the limited capacity of low energy structures to improve wake recovery.

Hussain (1986) wrote: 'the excitation amplitude should be small but sufficiently above the background disturbance or free stream turbulence' for organised structures to emerge from periodic excitation. This highlights a key requirement: although platform-induced excitations may be of low amplitude, they must remain distinguishable from the background turbulence to effectively influence wake dynamics. In this context, the energy ratio between free-stream turbulence and platform motion, $\epsilon^*_\infty/\epsilon^*_p$, emerges as a useful metric for assessing the conditions under which coherent structures can form and grow sufficiently to enhance recovery. Our results, illustrated in figures 13, 14, 15 and 16, reveal pronounced differences between the effects of surge (fore-aft) and sway (side-to-side) excitations on wake dynamics and recovery. For surge, when the energy of inflow turbulence approaches that of the platform motion, the wake fails to sustain coherent structures with sufficient energy to influence recovery. In contrast, sway-induced structures remain effective up to significantly higher turbulence levels, with $\epsilon^*_\infty/\epsilon^*_p \approx 3.5$. This suggests that meandering modes triggered by sway motion are either more easily excited, more robust against turbulent noise or both – making sway-induced excitations more persistent than their surge-induced (pulsating) counterparts under similar inflow conditions. To enhance practical applicability, it becomes essential to identify excitation methods that retain their influence on wake dynamics even under high $\epsilon^*_\infty/\epsilon^*_p$ where background turbulence dominates over platform motion, and to understand further the underlying flow mechanisms.

The fundamental differences between surge- and sway-induced wake structures, along with their varying resilience to inflow turbulence, raise important questions about the underlying mechanisms driving their formation. Previous studies by Kleine *et al.* (2022) and Wei *et al.* (2024) suggest that blade-tip vortices play a key role in the development of pulsating wake structures. As TI_∞ increases, however, tip vortices become destabilised by the background fluctuations, leading to their early breakdown in the wake (Neunaber *et al.* 2020; Porté-Agel *et al.* 2020). This raises the question: Could the breakdown of these disturbed tip vortices limit the ability of pulsating structures to form? In contrast, sway-induced meandering structures (as seen in figure 11) are more resilient in turbulent conditions, suggesting that their formation is less dependent on near-wake tip vortices. However, Biswas & Buxton (2024*a*) found that the hub vortex may also influence the development of meandering structures. These findings emphasise the need for further investigation into the local flow mechanisms behind the formation and stability of large-scale wake structures due to periodic excitations, and their relationship with near-wake flow structures, such as tip and hub vortices.

Furthermore, the origin of the energy feeding the excited large-scale structures remains a key question. Portela, Papadakis & Vassilicos (2020) showed that in the wake of a square obstacle, coherent structures are primarily energised by the mean flow. Analogous results were observed in the wake of a fixed wind turbine by Biswas & Buxton (2024*b*), who investigated energy exchanges in the near wake and identified the mean flow as the primary source of erratic wake meandering. A similar mechanism is likely at play in our case. Other contributions – such as from tip vortices, hub vortices or even inflow turbulence with the hypothesis of a backward energy cascade – may also be found. While a full analysis of these energy exchanges lies beyond the present scope, these aspects merit further investigation.

Our line measurements are limited in providing a full 3-D picture of the coherent structures, especially the meandering mode. It remains uncertain whether this mode forms as a helical structure or resembles a more von Kármán-like vortex, primarily driven by lateral motion with minimal vertical displacement. Additionally, it remains unclear whether meandering and pulsating wake modes emerge from a common system of interacting helical vortex structures, or if they represent fundamentally different vortex dynamics.

In the broader fluid dynamic context of transition to turbulence, our study shows similarities with other means of transition to turbulence in a flow. Figure 14 suggests a behaviour qualitatively similar to that observed downstream of passive fractal grids (Valente & Vassilicos 2011; Hearst & Lavoie 2014) and active grids (Mora, Obligado & Vassilicos 2019; Neuhaus *et al.* 2020). In both cases, flow structures (periodic in our case) initially gain energy at a rate determined by factors such as the direction of motion (which influences the type of flow structure), excitation energy (e.g. forcing amplitude or grid motion) and the inflow turbulence intensity TI_∞. As these structures accumulate energy while being advected downstream, they eventually become unstable, roughly at the point where the local turbulence level is highest, as observed in Messmer *et al.* (2024*a*). The destabilised, high-energy structures then decay, likely to small-scale eddies, feeding the turbulent cascade, similar to the mechanisms described by Mora *et al.* (2019) behind an active grid. Although grid-generated turbulence typically begins with a non-turbulent inflow, the underlying phenomena remain qualitatively similar to what is observed in turbine wake dynamics. From this perspective, a row of floating wind turbines within a wind farm can be seen as an array of independently actuated elements – analogous to shafts in an active grid – each capable of modulating the flow and potentially accelerating the transition to turbulence in the whole wake, offering potential applications for cluster wake control, as outlined by Gutknecht *et al.* (2024).

5.3. *Implication for wind energy*

The wake profiles and recovery results presented in figures 7 and 8 demonstrate that platform motion – or, more generally, periodic excitation strategies applied at the rotor level – can enhance wake recovery, particularly under low to moderate inflow turbulence conditions ($TI_\infty \leqslant 3{-}4\,\%$). From a wind energy perspective, this implies that downstream turbines can benefit from increased mean flow velocities when placed behind an upstream rotor undergoing periodic excitation at a Strouhal number $St \approx 0.3$. For instance, a 3 % increase in mean streamwise velocity ($\overline{u}$) was observed for sway excitation at $TI_\infty = 4.1\,\%$ (see figure 8*d*). This corresponds to a 9 % increase in available power ($\overline{u}^3$), eventually converted into electrical power by a potential downstream wind turbine, highlighting the industrial relevance of wake control strategies even under moderate turbulence intensity conditions.

Future studies should focus on optimising wake mixing at the wind farm scale. The current findings suggest that promoting wake meandering may be particularly effective in enhancing momentum recovery. This is especially relevant for floating wind turbines, which could be designed to naturally exhibit motion dynamics favouring wake mixing; e.g. oscillations near $St \approx 0.3$. However, the potential benefits must be carefully balanced against possible increases in structural loads. More broadly, the effectiveness of wake control strategies appears to diminish at higher inflow turbulence intensities ($TI_\infty > 5\,\%$), where natural turbulent mixing already promotes sufficient wake recovery. In such conditions, active control may either be energetically inefficient or require derating to achieve meaningful gains.

Last, this study did not analyse the influence of the largest-scale structures in the inflow, characterised by the integral length scale $\mathcal{L}_0$, on wake dynamics and recovery. These structures have been shown to be an important additional parameter influencing wake behaviour (Gambuzza & Ganapathisubramani 2023; Bourhis & Buxton 2024; Bourhis *et al.* 2025; Hodgson, Troldborg & Andersen 2025). Given the variability of large-scale structures that wind farms might encounter (Hodgson *et al.* 2025), the interaction between $\mathcal{L}_0$ and rotor-induced motion is of particular interest, especially in the context of wake meandering modelling. As discussed by Li *et al.* (2022), two primary mechanisms are typically considered for wake meandering. The first is passive advection, where large-scale inflow eddies passing through the rotor (typically having a size $\mathcal{L} > 2D$, corresponding to $St_\mathcal{L} = D/\mathcal{L} < 0.5$) displace the wake laterally and vertically, as described in the well-known dynamic wake meandering (DWM) model from Larsen *et al.* (2008). The second is shear-flow-induced meandering, where natural instabilities in the wake give rise to organised large-scale motions. These instabilities may arise naturally within the shear layer or be externally excited, as demonstrated in the present study, where platform sway induces large coherent meandering structures (figure 11) at the platform motion frequency, f_p.

The forced meandering observed here is highly amplified: platform motions with amplitudes of only about $2\,\%D$ generate lateral structures of span $\sim D$, and the associated energy amplification is substantial. For example, figure 13(*b*) (*b*.2) shows that the total energy in the coherent structure E^*_{CS} is approximately 30 times greater than the input excitation energy ϵ^*_p. This indicates a strong nonlinear response that is not captured by classical passive-advection-based models like DWM.

Our results suggest that, for inflow turbulence intensities $TI_\infty \lesssim 4\,\%$, shear-flow-induced meandering may play a dominant role in wake dynamics, especially when the rotor experiences forced excitations. Incorporating such nonlinear amplification effects into engineering models – for example, through low-order resolvent-based frameworks such as that proposed by Li & Yang (2024, 2025), or other methods – could improve predictions of structural loads and performance for downstream turbines. Finally, an improved understanding of the interplay between $\mathcal{L}_0$-driven meandering (i.e. passive advection, a primarily linear phenomenon) and shear-flow meandering (a nonlinear phenomenon), recently discussed by Bourhis *et al.* (2025), is of great interest. For $TI_\infty \lesssim 4\,\%$, wake meandering is likely driven by shear-flow instabilities, whereas increasing levels of TI_∞ lead to a reduced impact of shear instabilities and an increased impact of the linear effect of passive advection. The overlap, interaction and dependence on C_T, $\mathcal{L}_0$, TI_∞ and potentially the wake excitation strategy remain open questions that are of interest for improving models and predictions.

Acknowledgements. The authors would like to thank J. Jüchter, J. Maus, J. Puczylowski, K. Silwal, T. Wester, L. Ledoux and A. Hölling for their valuable help with the experiments in Oldenburg. Special thanks to S. Goedeke and L. Neuhaus for the support with the active grid. They also thank C. Messmer for the precious help with the transport of the set-up from Oldenburg to Milan. The authors are thankful to M. Montenegro

Montero and K. Yilmazlar for their great help with the experiments. Many thanks to L. Riccobene and D. Grassi for their technical support during the experiments in Milan.

The authors would like to acknowledge the assistance of ChatGPT (OpenAI) in refining the clarity and English language style of this paper. As non-native English speakers, this support helped improve the overall readability of the paper.

The authors wish to express their appreciation to the reviewers for their constructive critique and suggestions, which contributed meaningfully to the refinement of this work.

Lastly, the authors thank Martin Bourhis and Sandrine Aubrun for the helpful conversations over the past years and for their thoughtful input, which contributed to analyses and discussions.

Funding. This work has received funding from (i) the EU's Horizon 2020 research and innovation programme under the Marie Sklodowska–Curie grant agreement *N*°860879, as part of the FLOAWER consortium; (ii) the FLORIDA project, funded by the Deutsche Forschungsgemeinschaft (DFG, German Research Foundation) – *N*°529978479.

Declaration of interests. The authors report no conflict of interest.

Appendix A. Phase-averaging methodology

We briefly present the methodology used to compute $\widetilde{u_i}$ (see 2.4), the phase-averaged component of the wind speed signal with a period equal to the platform excitation, $T_p = 1/f_p$. This method applies to both the Milan dataset (3-D field) and the Oldenburg dataset (1-D field).

The goal is to compute $\widetilde{u_i}(\phi^*)$, a periodic function of a coherent mode at frequency f_k, identified in the wake. The phase satisfies $\phi(t) = \phi(t + 1/f_k)$ and is rescaled to a normalised phase via $\phi^* = (\phi(t) - \phi_0) \bmod 2\pi$. In this study we focus on $T_p = 1/f_p = D/(U_\infty St)$, but the methodology is applicable for any f_k for which the signal exhibits coherent energy (i.e. a distinct spectral peak; see Messmer *et al.* (2024*a*) for details).

To compute $\widetilde{u_i}(\phi^*)$, we implement the following steps (which we display in figure 17) using a Python algorithm that takes as input the fluctuating velocity field

$$u_i'(x, y, z, t) = u_i(x, y, z, t) - \overline{u_i(x, y, z, t)}, \quad \text{with } i = x, y, z. \tag{A1}$$

(i) Step 1: apply a low-pass filter to u_i' with cutoff frequency $f_{cut} \approx 3 f_k$ to isolate coherent fluctuations. Denote the filtered signal as u_i^{filt}.

(ii) Step 2: segment u_i^{filt} into bins of size $n_k = f_s/f_k$, where f_s is the sampling frequency. This results in approximately $N_{seg} = T_{meas} \cdot f_k$ segments, each corresponding to one period of the coherent mode. Since $N_{seg} \gg 10$ in all cases, phase averaging is statistically meaningful. The segmented signal is (see as an example the 20 segments in figure 17*a*):

$$u_i^{filt} = \left[u_i^{filt}(1),\ u_i^{filt}(2),\ \ldots,\ u_i^{filt}(n_k)\right] + \tag{A2}$$

$$\left[u_i^{filt}(n_k + 1),\ \ldots,\ u_i^{filt}(2n_k)\right] + \tag{A3}$$

$$\cdots + \tag{A4}$$

$$\left[u_i^{filt}(N_{seg} \cdot n_k),\ \ldots,\ u_i^{filt}((N_{seg} + 1) \cdot n_k)\right]. \tag{A5}$$

(iii) Step 3: compute the phase-averaged signal over all periods (figure 17*b*):

$$\widetilde{u_i^{filt}} = \Big[\left(u_i^{filt}(1) + u_i^{filt}(n_k + 1) + \cdots + u_i^{filt}(N_{seg} \cdot n_k + 1)\right)/N_{seg}, \tag{A6}$$

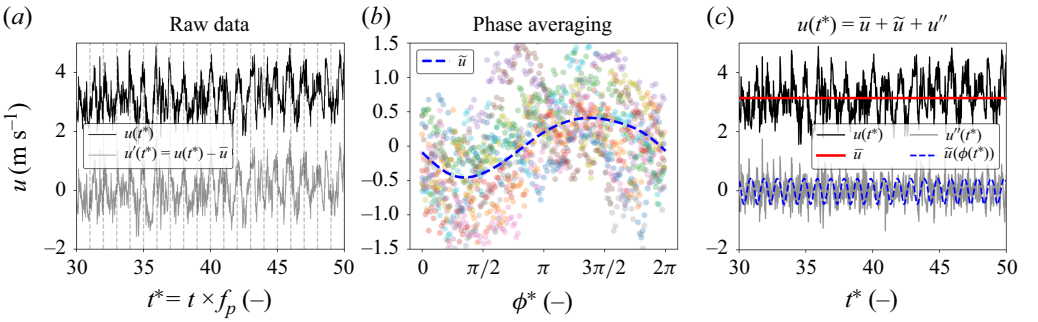

Figure 17. Visualisation of phase-averaging methodology. (*a*) Wake wind speed time series of the floating wind turbine partitioned in bins of size f_s/f_p, giving one bin per period $T_p = 1/f_p$ (step 2). (*b*) Superposition of the N_{seg} bins and phase averaged signal (step 3). (*c*) Raw signal decomposed as the sum of the mean, phase-averaged and stochastic fluctuations (2.4).

$$\left(u_i^{filt}(2) + u_i^{filt}(n_k + 2) + \cdots + u_i^{filt}(N_{seg} \cdot n_k + 2)\right)/N_{seg}, \tag{A7}$$

$$\ldots, \tag{A8}$$

$$\left(u_i^{filt}(n_k) + u_i^{filt}(2n_k) + \cdots + u_i^{filt}((N_{seg} + 1) \cdot n_k)\right)/N_{seg}\Big]. \tag{A9}$$

(iv) Finally, we define the discrete phase-averaged signal as $\widetilde{u_i}(\phi_k)$ with $\phi_k \in [\![0, n_k]\!]$, corresponding to $\phi^* \in [0, 2\pi]$ sampled at n_k points per cycle. The decomposition of (2.4) is displayed in figure 17(*c*).

Appendix B. Comparison of Milan and Oldenburg data and additional details about the computation of $\partial/\partial x_i$ terms and error estimation

In § 3.1 we use two datasets (corresponding to the cases fixed-5, surge-5 and sway-5 in table 2) to compute the recovery rate budget terms of (2.6). These datasets were obtained from experiments conducted in two different wind tunnels – Milan and Oldenburg – but great care was taken to replicate identical inflow and operating conditions across both facilities. To validate the comparability of the datasets, we present in figure 18(*a*) comparison of wake profiles of the mean streamwise wind speed (figure 18*a–e*) and streamwise velocity fluctuations (figure 18*f–j*), both normalised by the free-stream wind speed. Figure 18*a–e* show good agreement between the mean wake velocities measured in Milan (solid lines) and Oldenburg (semi-transparent dashed lines) across all three motion cases. The inter-experimental discrepancy, defined as the relative difference between datasets, $|\,(\overline{u}_M - \overline{u}_O)/\overline{u}_M\,|$, reaches a maximum of approximately 10 % at $x = 6D$ (figure 18*c*), while remaining below 5 % at most other downstream locations. For the velocity fluctuations (figures 18*f–j*), the relative difference between the two experiments is generally within 5 %, indicating a satisfactory level of consistency between the independently acquired datasets. To reflect the inter-experimental uncertainty between the two independent datasets, error bars corresponding to ±5 % were added to figure 4(*a*). Note that the intrinsic measurement uncertainty of hot-wire anemometry for an individual measurement, ϵ_{HW}, is considerably lower, estimated at approximately $\epsilon_{HW} \sim 2\,\%$ in Neunaber (2019) for similar experiments.

It is worth noting that the experiments in Milan were conducted on different days and even in different months depending on the downstream position: measurements at $x = 2D$,

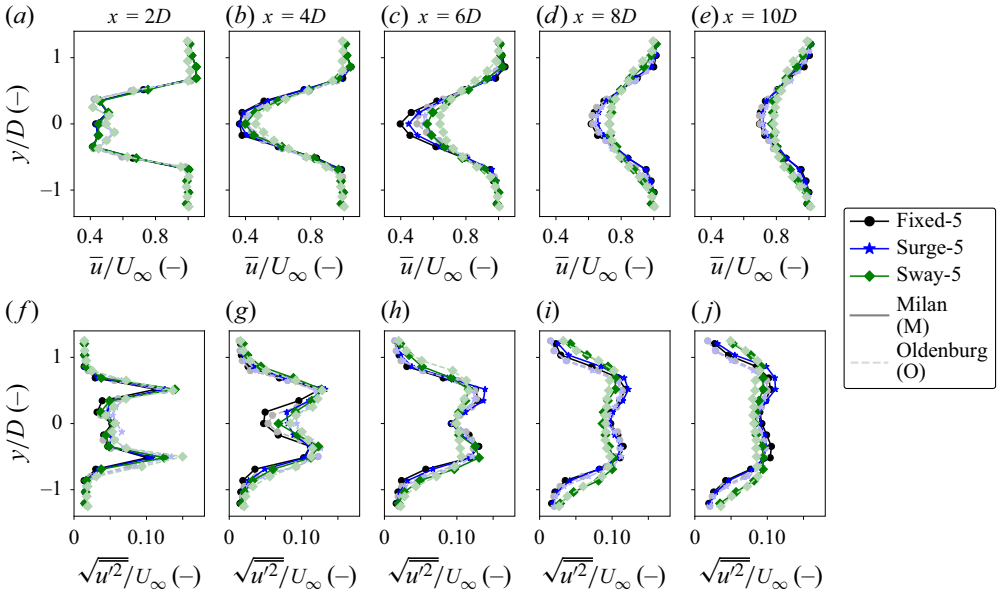

Figure 18. Comparison of Milan and Oldenburg datasets (fixed-5, surge-5 and sway-5 cases in table 2). (*a–e*) Horizontal profiles of the mean streamwise wind speed at $x \in [2D, 10D]$. (*f–j*) Horizontal profiles of the streamwise wind speed fluctuations at $x \in [2D, 10D]$. Both quantities are normalised by the free-stream velocity.

$6D$ and $10D$ were taken in March 2022, while those at $4D$ and $8D$ were performed in June 2022. This required resetting the experiment each time, resulting in slight variations in turbine and probe positioning as well as operating conditions. In contrast, the experiments in Oldenburg for all three cases were performed consecutively on the same day for $x \in [1.5D, 10D]$ under consistent operating conditions. As such, we expect the Oldenburg data to exhibit greater stability in the mean wind speed. The close agreement in velocity fluctuations between the Milan and Oldenburg datasets further validates our approach – namely, using Oldenburg data for recovery computation and Milan data for Reynolds stress terms – as the comparison of profiles in figure 18*f–j* indicates that the essential turbulent features are robust to minor experimental variations.

As a point of comparison, Aubrun *et al.* (2019) evaluated wake measurements of fixed porous and actuator disks across nine wind tunnel facilities worldwide under nominally identical inflow conditions. Despite the simplicity and standardisation of these tests, differences of up to 15 % were observed between facilities. These discrepancies are often attributed to numerous factors, including probe positioning, probe type and calibration, operating conditions (e.g. inflow turbulence intensity TI_∞, thrust coefficient C_T), yaw misalignment and reference wind speed. Even slight differences in these parameters between two experiments can cumulatively lead to variations in the results.

Given these considerations and looking at our results, the Milan and Oldenburg datasets are sufficiently consistent to be jointly analysed in this study.

The different terms in (2.6) involve derivatives of the mean flow field and Reynolds stresses in the x, y and z directions. To compute these terms, we used the Milan dataset for those involving $\partial/\partial y$ and $\partial/\partial z$. Specifically, we applied the numpy.gradient (*v2.1* at the time of the analysis) function in Python to the wake field, where the spatial resolution is Δy, $\Delta z = 0.34R$ – the spacing between measurement points (see figure 2*a*).

For derivatives in the streamwise direction, $\partial/\partial x$, we used the Oldenburg dataset, which provides data points at intervals of half a rotor diameter, i.e. $\Delta x = 0.5D$.

As mentioned in the manual of numpy.gradient: 'the gradient is computed using second order accurate central differences in the interior points and either first or second order accurate one-sides (forward or backwards) differences at the boundaries'. For the interior points (i.e. $x \in]2,\ 10[D$, $\{y, z\} \in]-1.34,\ 1.34[R$,), the derivative of a given $\overline{g}(x,\ y,\ z)$ is computed as

$$\frac{\partial \overline{g}}{\partial x} \approx \frac{\overline{g}(x+\Delta x,\ y,\ z) - \overline{g}(x-\Delta x,\ y,\ z)}{2\Delta x} + \mathcal{O}(\Delta x^2), \quad \Delta x = 0.5D, \tag{B1}$$

$$\frac{\partial \overline{g}}{\partial y} \approx \frac{\overline{g}(x,\ y+\Delta y,\ z) - \overline{g}(x,\ y-\Delta y,\ z)}{2\Delta y} + \mathcal{O}(\Delta y^2), \quad \Delta y = 0.17D, \tag{B2}$$

$$\frac{\partial \overline{g}}{\partial z} \approx \frac{\overline{g}(x,\ y,\ z+\Delta z) - \overline{g}(x,\ y,\ z-\Delta z)}{2\Delta z} + \mathcal{O}(\Delta z^2), \quad \Delta z = 0.17D. \tag{B3}$$

The resulting recovery rate budget shown in figure 6 balances well, especially in the far wake ($x \geqslant 8D$, where the pressure and rotation terms are null), supporting the assumption that the spatial resolution in all three directions is sufficient. Thus, we consider the finite-difference approximation $\partial\overline{g}/\partial x_i \approx \Delta\overline{g}/\Delta x_i$ to be appropriate for our computations.

To quantify the uncertainty in spatial derivatives, we employed a Monte Carlo uncertainty propagation method, similar to the approach of Rezaeiravesh *et al.* (2018). A total of $N_{MC} > 10^3$ synthetic realisations of each measured quantity $\overline{g}(x,\ y,\ z)$ were generated by perturbing the original data with Gaussian noise. The noise amplitude corresponded to a typical hot-wire measurement uncertainty of $\epsilon_{HW} = 2\,\%$, consistent with values reported in previous experimental studies (e.g. (Neunaber 2019)). For each realisation, the gradient $\partial\overline{g}/\partial x_i$ was computed using the numpy.gradient function. The standard deviation across the ensemble of synthetic gradients was then taken as the estimated uncertainty in the derivative. On average, the resulting uncertainty in the various mean flow and Reynolds stress derivative terms (e.g. $\partial\overline{u}/\partial x$, $\partial\overline{u'v'}/\partial y$, etc.) is approximately $\epsilon_{\partial/\partial x_i} = 15\,\%$, as shown in figure 4(*b*) for the example of $D\langle\partial\overline{u}/\partial x\rangle$. This Monte Carlo-based uncertainty estimate supports the interpretation of the derivative terms presented in figures 5 and 6, which can be assumed to carry an error margin of approximately $\epsilon_{\partial/\partial x_i} = 15\,\%$.

References

Alves Portela, F., Papadakis, G. & Vassilicos, J.C. 2020 The role of coherent structures and inhomogeneity in near-field interscale turbulent energy transfers. *J. Fluid Mech.* **896**, A16.

Angelou, N., Mann, J. & Dubreuil-Boisclair, C. 2023 Revealing inflow and wake conditions of a 6 MW floating turbine. *Wind Energy Sci.* **8** (10), 1511–1531.

Aubrun, S. *et al.* 2019 Round-robin tests of porous disc models. *J. Phys. Conf. Ser.* **1256**, 012004.

Baj, P., Bruce, P.J.K. & Buxton, O.R.H. 2015 The triple decomposition of a fluctuating velocity field in a multiscale flow. *Phys. Fluids* **27** (7), 075104-1–075104-24.

Bastankhah, M. & Porté-Agel, F. 2014 A new analytical model for wind-turbine wakes. *Renew. Energy* **70**, 116–123.

Bastankhah, M. & Porté-Agel, F. 2016 Experimental and theoretical study of wind turbine wakes in yawed conditions. *J. Fluid Mech.* **806**, 506–541.

Biswas, N. & Buxton, O.R.H. 2024*a* Effect of tip speed ratio on coherent dynamics in the near wake of a model wind turbine. *J. Fluid Mech.* **979**, A34.

Biswas, N. & Buxton, O.R.H. 2024*b* Energy exchanges between coherent modes in the near wake of a wind turbine model at different tip speed ratios. *J. Fluid Mech.* **996**, A8.

Bossuyt, J., Ferčák, O., Sadek, Z., Meneveau, C., Gayme, D. & Cal, R.B. 2023 Floating wind farm experiments through scaling for wake characterization, power extraction, and turbine dynamics. *Phys. Rev. Fluids.* **8** (12), 120501-1–120501-39.

BOUDREAU, M. & DUMAS, G. 2017 Comparison of the wake recovery of the axial-flow and cross-flow turbine concepts. *J. Wind Eng. Ind. Aerodyn.* **165**, 137–152.
BOURHIS, M. & BUXTON, O.R.H. 2024 Influence of freestream turbulence and porosity on porous disk-generated wakes. *Phys. Rev. Fluids* **9** (12), 124501.
BOURHIS, M., MESSMER, T., HÖLLING, M. & BUXTON, O.R.H. 2025 Impact of freestream turbulence and thrust coefficient on wind turbine-generated wakes. arXiv: 2503.21903.
CANNON, S., CHAMPAGNE, F. & GLEZER, A. 1993 Observations of large-scale structures in wakes behind axisymmetric bodies. *Exp. Fluids* **14** (6), 447–450.
CANTWELL, B. & COLES, D. 1983 An experimental study of entrainment and transport in the turbulent near wake of a circular cylinder. *J. Fluid Mech.* **136**, 321–374.
CHEUNG, L.C., BROWN, K.A., HOUCK, D.R. & DEVELDER, N.B. 2024 Fluid-dynamic mechanisms underlying wind turbine wake control with Strouhal-timed actuation. *Energies* **17** (4), 865.
CROCE, A., CACCIOLA, S., MONTERO MONTENEGRO, M., STIPA, S. & PRATICÓ, R. 2023 A CFD-based analysis of dynamic induction techniques for wind farm control applications. *Wind Energy* **26** (3), 325–343.
CROW, S.CJ & CHAMPAGNE, F.H. 1971 Orderly structure in jet turbulence. *J. Fluid Mech.* **48** (3), 547–591.
DA SILVA, C.B., HUNT, J.C.R., EAMES, I. & WESTERWEEL, J. 2014 Interfacial layers between regions of different turbulence intensity. *Annu. Rev. Fluid Mech.* **46**, 567–590.
FONTANELLA, A., FUSETTI, A., CIONI, S., PAPI, F., MUGGIASCA, S., PERSICO, G., DOSSENA, V., BIANCHINI, A. & BELLOLI, M. 2025 Wake development in floating wind turbines: new insights and an open dataset from wind tunnel experiments. *Wind Energy Sci.* **10** (7), 1369–1387.
FONTANELLA, A., ZASSO, A. & BELLOLI, M. 2022 *Wind tunnel investigation of the wake-flow response for a floating turbine subjected to surge motion*. *J. Phys.: Conf. Ser.* **2265**, 042023.
FREDERIK, J., DOEKEMEIJER, B., MULDERS, S. & VAN WINGERDEN, J. 2020 The helix approach: using dynamic individual pitch control to enhance wake mixing in wind farms. *Wind Energy* **23** (8), 1739–1751.
FU, S., JIN, Y., ZHENG, Y. & CHAMORRO, L.P. 2019 Wake and power fluctuations of a model wind turbine subjected to pitch and roll oscillations. *Appl. Energy* **253**, 113605.
FUENTES NORIEGA, E. & MAZELLIER, N. 2025 Scaling analysis of the swirling wake of a porous disc: application to wind turbines. *J. Fluid Mech.* **1003**, A34.
GAMBUZZA, S. & GANAPATHISUBRAMANI, B. 2023 The influence of free stream turbulence on the development of a wind turbine wake. *J. Fluid Mech.* **963**, A19.
GUPTA, V. & WAN, M. 2019 Low-order modelling of wake meandering behind turbines. *J. Fluid Mech.* **877**, 534–560.
GUTKNECHT, J., BECKER, M., TASCHNER, E., STIPA, S., ALLAERTS, D., VIRÉ, A. & VAN WINGERDEN, J.-W. 2024 Active cluster wake mixing. *J. Phys.: Conf. Ser.* **2767**, 092052.
HEARST, R.J. & LAVOIE, P. 2014 Decay of turbulence generated by a square-fractal-element grid. *J. Fluid Mech.* **741**, 567–584.
HO, C.M. & HUERRE, P. 1984 Perturbed free shear layers. *Annu. Rev. Fluid Mech.* **16**, 365–424.
HODGSON, E.L., MADSEN, M. H.A. & ANDERSEN, S.J. 2023 Effects of turbulent inflow time scales on wind turbine wake behavior and recovery. *Phys. Fluids* **35** (9), 095125-1–095125-21.
HODGSON, E.L., TROLDBORG, N. & ANDERSEN, S.J. 2025 Impact of freestream turbulence integral length scale on wind farm flows and power generation. *Renew. Energy* **238**, 121804.
HUBERT, A., CONAN, B. & AUBRUN, S. 2025 Spatiotemporal behavior of the far wake of a wind turbine model subjected to harmonic motions: phase averaging applied to stereo particle image velocimetry measurements. *Wind Energy Sci.* **10** (7), 1351–1368.
HUSSAIN, A.K.M.F. 1986 Coherent structures and turbulence. *J. Fluid Mech.* **173**, 303–356.
KANKANWADI, K.S. & BUXTON, O.R.H. 2020 Turbulent entrainment into a cylinder wake from a turbulent background. *J. Fluid Mech.* **905**, A35.
KLEINE, V.G., FRANCESCHINI, L., CARMO, B.S., HANIFI, A. & HENNINGSON, D.S. 2022 The stability of wakes of floating wind turbines. *Phys. Fluids* **34** (7), 074106-1–074106-21.
KORB, H., ASMUTH, H. & IVANELL, S. 2023 The characteristics of helically deflected wind turbine wakes. *J. Fluid Mech.* **965**, A2.
LARSEN, G.C., MADSEN, H.A., THOMSEN, K. & LARSEN, T.J. 2008 Wake meandering: a pragmatic approach. *Wind Energy*, **11** (4), 377–395.
LI, Y.T., YU, W. & SARLAK, H. 2024 Wake structures and performance of wind turbine rotor with harmonic surging motions under laminar and turbulent inflows. *Wind Energy* **27** (12), 1499–1525.
LI, Z., DONG, G. & YANG, X. 2022 Onset of wake meandering for a floating offshore wind turbine under side-to-side motion. *J. Fluid Mech.* **934**, A29.
LI, Z. & YANG, X. 2024 Resolvent-based motion-to-wake modelling of wind turbine wakes under dynamic rotor motion. *J. Fluid Mech.* **980**, A48.

LI, Z. & YANG, X. 2025 Self-consistent model for active control of wind turbine wakes. *J. Fluid Mech.* **1013**, A36.

LIGNAROLO, L E M., RAGNI, D., SCARANO, F., SIMÃO FERREIRA, C J. & VAN BUSSEL, G J W. 2015 Tip-vortex instability and turbulent mixing in wind-turbine wakes. *J. Fluid Mech.* **781**, 467–493.

MAO, X. & SØRENSEN, J.N. 2018 Far-wake meandering induced by atmospheric eddies in flow past a wind turbine. *J. Fluid Mech.* **846**, 190–209.

MESSMER, T., BRIGDEN, C., PEINKE, J. & HÖLLING, M. 2022 A six degree-of-freedom set-up for wind tunnel testing of floating wind turbines. *J. Phys.: Conf. Ser.* **2265**, 042015.

MESSMER, T., HÖLLING, M. & PEINKE, J. 2024*a* Enhanced recovery caused by nonlinear dynamics in the wake of a floating offshore wind turbine. *J. Fluid Mech.* **984**, A66.

MESSMER, T., PEINKE, J. & HÖLLING, M. 2024*b* Wind tunnel investigation on the recovery and dynamics of the wake of a floating offshore wind turbine subjected to low inflow turbulence. *J. Phys.; Conf. Ser* **2767**, 092083.

MORA, D.O., MUÑIZ PLADELLORENS, E., RIERA TURRÓ, P., LAGAUZERE, M. & OBLIGADO, M. 2019 Energy cascades in active-grid-generated turbulent flows. *Phys. Rev. Fluids* **4** (5), 054602.

MÜHLE, F.V., TAMARO, S., KLINGER, F., CAMPAGNOLO, F. & BOTTASSO, C.L. 2024 *Experimental and numerical investigation on the potential of wake mixing by dynamic yaw for wind farm power optimization*. *J. Phys.: Conf. Ser.* **2767**, 092068.

MUNTERS, W. & MEYERS, J. 2018 Towards practical dynamic induction control of wind farms: analysis of optimally controlled wind-farm boundary layers and sinusoidal induction control of first-row turbines. *Wind Energy Sci.* **3** (1), 409–425.

NEUHAUS, L., BERGER, F., PEINKE, J. & HÖLLING, M. 2021 Exploring the capabilities of active grids. *Exp. Fluids* **62** (6), 130.

NEUHAUS, L., HÖLLING, M., BOS, W.J. T. & PEINKE, J. 2020 Generation of atmospheric turbulence with unprecedentedly large Reynolds number in a wind tunnel. *Phys. Rev. Lett.* **125** (15), 154503.

NEUNABER, I. 2019 Stochastic investigation of the evolution of small-scale turbulence in the wake of a wind turbine exposed to different inflow conditions. *PhD thesis*, Universität Oldenburg, Germany.

NEUNABER, I., HÖLLING, M., STEVENS, R.J.A.M., SCHEPERS, G. & PEINKE, J. 2020 Distinct turbulent regions in the wake of a wind turbine and their inflow-dependent locations: the creation of a wake map. *Energies* **13** (20), 5392.

OSTER, D. & WYGNANSKI, I. 1982 The forced mixing layer between parallel streams. *J. Fluid Mech.* **123**, 91–130.

PAGAMONCI, L., PAPI, F., COJOCARU, G., BELLOLI, M. & BIANCHINI, A. 2025 How does turbulence affect wake development in floating wind turbines? A critical assessment. *Wind Energy Sci. Discuss.* **2025**, 1–36.

PIKOVSKY, A., ROSENBLUM, M. & KURTHS, J. 2001, *Synchronization*. Cambridge University Press.

PLATIS, A., HUNDHAUSEN, M., LAMPERT, A., EMEIS, S. & BANGE, J. 2021 The role of atmospheric stability and turbulence in offshore wind-farm wakes in the German bight. *Boundary Layer Meteorol.* 1–29.

POPE, S.B. 2001 Turbulent flows. *Meas. Sci. Technol.* **12** (11), 2020–2021.

PORTÉ-AGEL, F., BASTANKHAH, M. & SHAMSODDIN, S. 2020 Wind-turbine and wind-farm flows: a review. *Boundary-Layer Meteorol.* **174** (1), 1–59.

RAMOS-GARCÍA, N., KONTOS, S., PEGALAJAR-JURADO, A., GONZÁLEZ HORCAS, S. & BREDMOSE, H. 2022 Investigation of the floating IEA Wind 15 MW RWT using vortex methods. Part I: Flow regimes and wake recovery. *Wind Energy* **25** (3), 468–504.

REYNOLDS, W.C. & HUSSAIN, A.K.M.F. 1972 The mechanics of an organized wave in turbulent shear flow. Part 3. Theoretical models and comparisons with experiments. *J. Fluid Mech.* **54** (2), 263–288.

REZAEIRAVESH, S., VINUESA, R., LIEFVENDAHL, M. & SCHLATTER, P. 2018 Assessment of uncertainties in hot-wire anemometry and oil-film interferometry measurements for wall-bounded turbulent flows. *Eur. J. Mech. B/Fluids* **72**, 57–73.

ROBERTSON, A., JONKMAN, J., MASCIOLA, M., SONG, H, GOUPEE, A., COULLING, A. & LUAN, C. 2014 Definition of the semisubmersible floating system for phase II of OC4. Tech. Rep, National Renewable Energy Lab (NREL).

ROCKEL, S., PEINKE, J., HÖLLING, M. & CAL, R.A.B. 2017 Dynamic wake development of a floating wind turbine in free pitch motion subjected to turbulent inflow generated with an active grid. *Renew. Energy* **112**, 1–16.

SCHLIFFKE, B., CONAN, B. & AUBRUN, S. 2024 Floating wind turbine motion signature in the far-wake spectral content – a wind tunnel experiment. *Wind Energy Sci.* **9** (3), 519–532.

VALENTE, P.C. & VASSILICOS, J.C. 2011 The decay of turbulence generated by a class of multiscale grids. *J. Fluid Mech.* **687**, 300–340.

VAN DEN BERG, D., DE TAVERNIER, D. & VAN WINGERDEN, J.-W. 2023 The dynamic coupling between the pulse wake mixing strategy and floating wind turbines. *Wind Energy Sci.* **8** (5), 849–864.

VAN DER HOEK, D., DEN ABBEELE, B.V., SIMAO FERREIRA, C. & VAN WINGERDEN, J-W. 2024 Maximizing wind farm power output with the helix approach: experimental validation and wake analysis using tomographic particle image velocimetry. *Wind Energy* **27** (5), 463–482.

VAN DER LAAN, M.P., BAUNGAARD, M. & KELLY, M. 2023 Brief communication: a clarification of wake recovery mechanisms. *Wind Energy Sci.* **8** (2), 247–254.

WEI, N.J., EL MAKDAH, A., HU, J.C., KAISER, F., RIVAL, D.E. & DABIRI, J.O. 2024 Wake dynamics of wind turbines in unsteady streamwise flow conditions. *J. Fluid Mech.* **1000**, A66.

WYGNANSKI, I., CHAMPAGNE, F. & MARASLI, B. 1986 On the large-scale structures in two-dimensional, small-deficit, turbulent wakes. *J. Fluid Mech.* **168**, 31–71.

YILMAZ, A.E. & MEYERS, J. 2018 Optimal dynamic induction control of a pair of inline wind turbines. *Phys. Fluids* **30** (8), 085106-1–085106-20.